Ernst-Moritz-Arndt University of Greifswald

Master Thesis

Kinetic Effects in RF Discharges

Author:
Philipp Hacker

Supervisor:
Prof. Dr. Ralf Schneider
Examiner:
Prof. Dr. Jürgen Meichsner

A thesis submitted in fulfillment of the requirements for the degree of Master of Science - Physics

in the research group of

Computational Sciences,
Institute of Physics

September 2017

Declaration of Authorship

I hereby certify that this thesis has been composed by me and is based on my own work, unless stated otherwise. No other person's work has been used without due acknowledgement in this thesis. All references and verbatim extracts have been quoted, and all sources of information, including graphs and data sets, have been specifically acknowledged.

.....

Signature of author

Greifswald; September 2017

Contents

List of Abbreviations

abbreviation	**full expression**
e.g.	exempli gratia; *for example*
etc.	et cetera; *and so on*
ac, AC	alternating current
dc, DC	direct current
rf, RF	radio frequency
ccrf, CCRF	capacitively coupled radio frequency
EDF	*german: Energieverteilungsfunktion*, energy distribution function
EEDF, EED	electron energy distribution function
IEDF, IED	ion energy distribution function
p., pp.	page, plural pages
ff.	folio; *on the (next) page*, ablative of folium (*page*)
SIE, SEE	secondary ion/electron emission
HWA	hard wall approximation
MS	mass spectrometer
PROES	phase resolved optical emission spectroscopy
MWI	microwave interferometer
AN	antenna
FC	flow controller

abbreviation	**full expression**
PIC	particle-in-cell
MCC	Monte-Carlo-Colissions
1d3v, 2d3v	one/two spatial and three velocity dimensions

Table 1: List of abbreviations and their corresponding phrases. If specified, the translation or an equivalent expression is written.

Physical Quantities

Quantity	**Unit**	**Symbol**	**Dimension**	**Value**
Speed of Light	m/s	c_0	$\mathrm{L}^1\mathrm{T}^{-1}$	$2.997 \cdot 10^8$
thermal velocity	m/s	$v_{\mathrm{th,j}}$	$\mathrm{L}^1\mathrm{T}^{-1}$	
drift velocity	m/s	$v_{\mathrm{D,j}}$, u_{j}	$\mathrm{L}^1\mathrm{T}^{-1}$	
Boltzmann constant	eV/K	k_{B}	$\mathrm{M}^1\mathrm{L}^2\mathrm{T}^{-2}\mathrm{K}^{-1}$	$8.617 \cdot 10^{-23}$
mobility	cm^2/Vs	μ_{j}	$\mathrm{I}^1\mathrm{T}^2\mathrm{M}^{-1}$	
Planck constant	eVs	$\hbar$	$\mathrm{G}^{-1/2}\mathrm{c}^{6/2}\varepsilon_0^{1/2}$	$4.1345 \cdot 10^{-15}$ eVs $6.646 \cdot 10^{-34}$ Js
kinetic temperature	eV	T_{j}	$\mathrm{M}^1\mathrm{L}^2\mathrm{T}^{-2}$	$1\,\mathrm{eV} = 1.902 \cdot 10^{-19}\,\mathrm{K}$
elementary charge	C	e	$\mathrm{I}^1\mathrm{T}^1$	$1.902 \cdot 10^{-19}$
electric charge	C	Q, q	$\mathrm{I}^1\mathrm{T}^1$	
particle mass	kg	m_{j}	M^1	electron: $9.109 \cdot 10^{-31}$ ion: $5.310 \cdot 10^{-26}$ anion: $5.143 \cdot 10^{-26}$
reduced mass	kg	$\mu_{\mathrm{j,k}}$	M^1	
distance, location	cm	r, z, x, $\vec{r}$	L^1	
Debye length	cm	$\lambda_{\mathrm{D,j}}$	L^1	
particle distance	cm	$\overline{b}$	L^1	
mean free path	cm	$s_{\mathrm{mfp,j}}$	L^1	
particle density	cm^{-3}	n_{j}	L^{-3}	

Quantity	**Unit**	**Symbol**	**Dimension**	**Value**
Vacuum permittivity	F/m	ε_0	$\mathrm{M}^{-1}\mathrm{L}^{-3}\mathrm{T}^{-4}\mathrm{A}^2$	$8.854 \cdot 10^{-12}$
electrostatic potential	V	Φ, U	$\mathrm{M}^1\mathrm{L}^2\mathrm{I}^{-1}\mathrm{T}^{-3}$	
electric current	A	I, J	I^1	
electric current density	$\mathrm{A/cm}^2$	j_j	$\mathrm{I}^1\mathrm{L}^{-2}$	
electric charge density	$\mathrm{C/cm}^3$	ρ	$\mathrm{I}^1\mathrm{T}^1\mathrm{L}^{-3}$	
electric resistance	Ω	R	$\mathrm{M}^1\mathrm{L}^2\mathrm{T}^{-3}\mathrm{I}^{-2}$	
electric capacity	F	C	$\mathrm{M}^{-1}\mathrm{L}^{-2}\mathrm{T}^4\mathrm{I}^2$	
time	s	t	T^1	
plasma frequency	Hz	$\omega_{\mathrm{p,j}}$	T^{-1}	
collision frequency	Hz	ν_j	T^{-1}	

Table 2: Physical properties in their commonly — or for this purpose most convenient — units and corresponding SI units. If not specified, the values of each quantity refer to the afore-mentioned units.

Motivation

Reactive plasmas are a common tool in many industrial and scientific applications, such as semiconductor and computer chip production. Of high importance for the surface treatment are etching and sputtering processes [2, 26]. Especially in electronegative discharges sputter and deposition rates are increased. They depend crucially on the distribution function of impinging ions. Therefore, a detailed understanding of these distribution functions is needed to optimise the processes. Capacitively coupled discharges with radio-frequency modulated voltages (ccrf) have high-energy ions impinging on the electrodes. Their advantage is the absence of a net current onto the target, which preserves the structure of the product.

Laboratory experiments with ccrf oxygen discharges at low pressures and temperatures show a high-energy peak in the energy distribution function (EDF) of negative ions impinging on the anode. The position of this peak depends on the

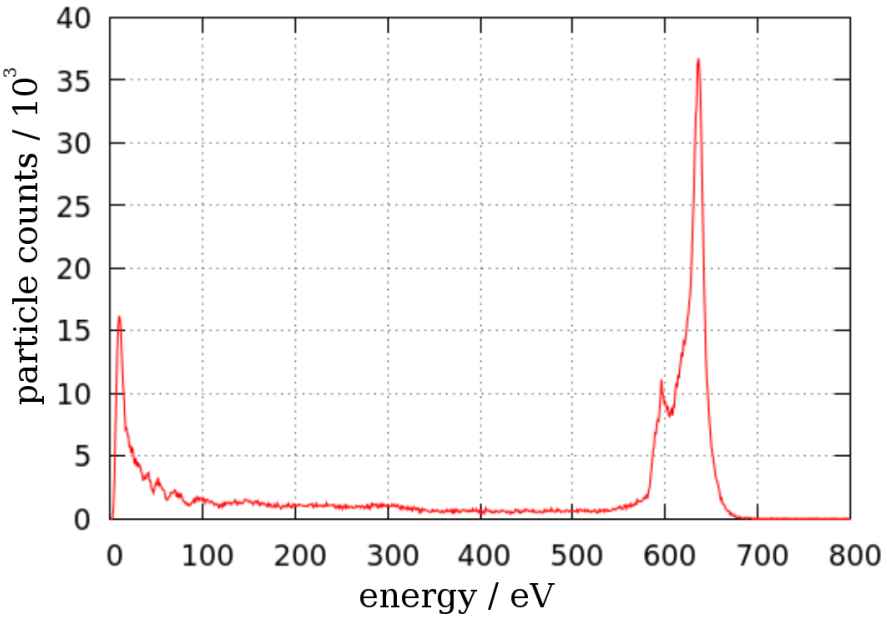

Figure 1: Experimentally measured anion energy distribution function impinging on the grounded electrode. Magnesium oxide was used as cathode material, which was powered with 50 W [19].

electrode material [19]. Experimentally measured anion EDF is shown in figure 1. A possible explanation is proposed by Stoffels and Kawano et al. [21, 8]: negative ions are produced by ionisation close to or at the surface of the electrode. The drawback of this theory is the lack of experimental or theoretical ionisation probabilities for anions at metal surfaces. Until now an explanation for this characteristic feature of the EDF of negative ions at the anode is missing.
In my thesis I will try to study this system and to improve the understanding of the underlying physics of the high-energy peak in the EDF of negative ions at a grounded electrode. Since the EDF is non-Maxwellian, a kinetic model is needed. Therefore, a Particle-in-Cell (PIC) code with Monte-Carlo-Collisions (MCC) is used to model the asymmetric ccrf discharges of low-temperature oxygen plasmas. In particular, an surface ionisation module for negative ions is introduced in the simulation and its effect on the EDF is studied.
In this thesis I will try to answer the following questions:

1. What determines the physics of ccrf low pressure oxygen plasmas?
2. What is the influence of surface processes on the distribution function of negative ions?

Numerical investigations of electronegative plasmas have been done, e.g. by [14, 1, 12] using an one-dimensional PIC model. It has proven to be a great tool for fundamental studies of reactive radio frequency plasmas. Although this is a good approach for the investigation of axial distribution functions of plasma species close to the axis, the 1D simulations lacks effects of radial transport, asymmetry and plasma-wall interaction. For these topics, a 2D radial-axial model is needed, which is validated by comparison with the existing 1D code. In the 2D model, additional effects, such as voltage offset *self bias* in ccrf discharges and asymmetry effects are taken into account.

To be able to answer the basic scientific question formulated before, I will firstly introduce the basic physics of plasmas in front of walls, the so-called plasma sheath. This will be extended to ccrf conditions, where the plasma reacts dynamically to the RF heating. The need for kinetic models to resolve the full distribution functions of all plasma species is satisfied by the PIC-MCC simulation method, which will be summarised shortly. As a part of the computational model, the relevant collision processes for such ccrf oxygen plasmas are discussed. In the second part of the thesis I will simulate the axial centre of the discharge without asymmetry effects using the one-dimensional model. These results are

also used for a validation of the 2D radial-axial model. After its successful validation the 2D model is used to simulate the experimental conditions of the plasma discharge from [19]. In the PIC simulations, special emphasis lies on the investigation of surface and asymmetry effects and their impacts. Finally, the work is summarised.

Chapter 1

Physical Properties of Low Temperature RF Plasmas

In this first chapter I will provide the necessary physical background for this work about the numerical simulation of low temperature, capacitively coupled radio frequency plasmas. Here I will firstly highlight the fundamental physics of a plasma and the interaction with walls. Upon that I will show the important features of asymmetric and capacitively coupled radio frequency discharges. Next the PIC simulation method with Monte-Carlo-Collision algorithms will be introduced. At last the necessary plasma chemistry and selected reaction set of oxygen will be presented.
An important aspect of oxygen plasmas is the existence of negative ions in addition to electrons. Therefore, a negatively charged species with large mass exists in addition to the electrons. The ratio between anion and electron density is defined as electronegativity $\eta = n_{\mathrm{i}^-}/n_{\mathrm{e}}$. This can range between 0.03–4 [9] for the oxygen plasmas considered in this thesis. One key question to be addressed is the influence of negative ions on the physics of the plasma.

1.1 Plasma Physics

The experiment studied in this work is a capacitively coupled radio frequency (ccrf) discharge with a low temperature plasma, operated at low pressures. A plasma is a globally quasi-neutral gas, consisting of freely moving charges — e.g. electrons, positive and negative ions — with additional neutral gas particles. It is characterised by the collective behaviour of the charged species. The ratio of ion particle density (n_{i}) and of the sum of neutral (n_{n}) and ion densities defines

the degree of ionisation. This is rather low for ccrf discharges, typically below 1%.

Charge separation of electrons and ions, and therefore the violation of the quasi-neutrality condition $n_\mathrm{e} = n_\mathrm{i}$ (electron density equals ion density), is only possible for distances below the *Debye length* λ_D. Regions where the quasi-neutrality condition is satisfied are called plasma bulk. The definition of the degree of ionisation α and the Debye length are:

$$\alpha = \frac{n_\mathrm{i}}{n_\mathrm{n} + n_\mathrm{i}}\,, \qquad \lambda_\mathrm{D}^2 = \left(\lambda_\mathrm{D,e}^{-2} + \lambda_\mathrm{D,i}^{-2}\right)^{-1}, \qquad \lambda_\mathrm{D,j}^2 = \frac{\varepsilon_0 k_\mathrm{B} T_\mathrm{j}}{n_\mathrm{j} e^2}\,. \tag{1.1}$$

where $\lambda_\mathrm{D,j}$ are the individual Debye lengths of the species j. This is also the characteristic scale beyond which the electric potential of a charge is fully shielded.

The creation of a plasma is accomplished by two parallel metal electrodes, where on at least one an ac or dc signal is applied. In this thesis I will consider alternating currents at radio frequency, 13.56 MHz with an amplitude between 100–1000 V.

The electrons are of a much smaller mass in comparison to the other plasma species, which is why they are at least $\sqrt{m_\mathrm{i}/m_\mathrm{e}}$ – times faster than ions and neutrals. Therefore they have a much higher mobility μ_e and thermal velocity $v_\mathrm{th,e}$. For the case of a plasma in front of a surface the larger mobility of electrons lead to an accumulation of a negative charge. To guarantee zero total current to the surface for a steady state, a negative potential drop with respect to the plasma bulk develops in front of the wall to reflect most of the electrons and balance

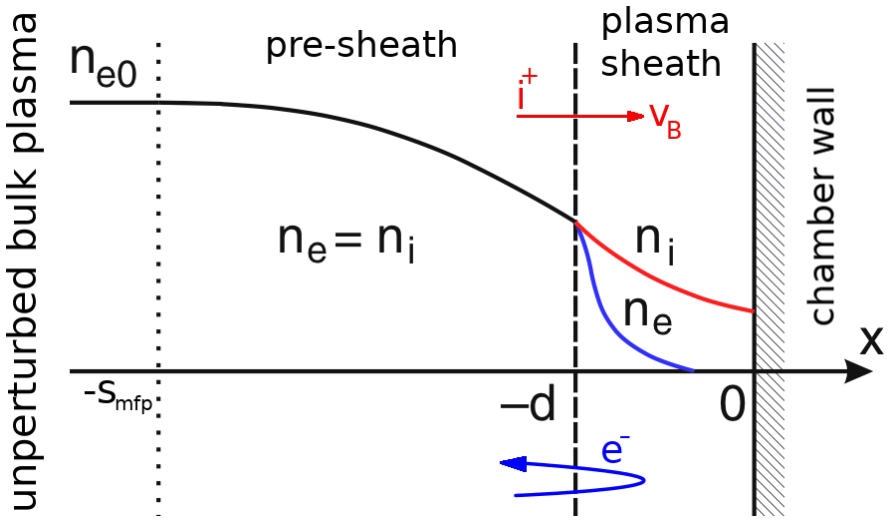

Figure 1.1: One dimensional density profiles as a function of the distance to a floating wall. Note the exponential decrease of the electron density n_e from the sheath border towards the negatively charged wall. Densities already reach approximately $0.66{\cdot}n_{\mathrm{e},0}$ inside the pre-sheath. [18]

electron and ion currents. A spatially restricted area called *plasma sheath* is established, where the electrons depletion occurs and ions are accelerated towards the wall. The characteristic scale is obviously on the order of some Debye scales, otherwise such a charge separation would not be possible.
The electron density $n_\mathrm{e}(x)$ towards the wall is given by the *Boltzmann* distribution function $f_\mathrm{B}(\Phi) \sim \exp(e\Delta\Phi/k_\mathrm{B}T_\mathrm{e})$ [18]. This means that the electron density decreases exponentially towards the negatively charged wall. It can be assumed that the sheath thickness d is much smaller than the mean free path of the ions ($d \ll s_\mathrm{mfp,i}$) inside the plasma bulk. Hence the ions enter the pre-sheath collisionless at a speed $v_\mathrm{i,0}$. The ion and electron densities are therefore:

$$n_\mathrm{i}(x) = n_\mathrm{i}(d)\left(1 - \frac{2e\Phi(x)}{m_\mathrm{i}v_\mathrm{i,0}^2}\right)^{-1/2} \quad \text{and} \quad n_\mathrm{e} = n_\mathrm{e}(d)\exp\left(\frac{e(\Phi(x)-\Phi(d))}{k_\mathrm{B}T_\mathrm{e}}\right). \tag{1.2}$$

One can assume that the kinetic energy of the ions at the sheath entrance is smaller than their potential energy, e.g. $m_\mathrm{i}v_\mathrm{i,0}^2 \ll |e\Phi(x)|$. Using *Poisson's* equation gives an expression for the potential $\Phi(x)$. Solving this, and using the unperturbed ion current $j_\mathrm{i} = n_\mathrm{i}(d)ev_\mathrm{i,0}$, one yields the result by *Langmuir* in equation 1.3:

$$\Delta\Phi \cong -\frac{en_\mathrm{i}(-d)}{\varepsilon_0}\left(-\frac{2e\Phi(x)}{m_\mathrm{i}v_\mathrm{i,0}^2}\right)^{-\frac{1}{2}} \quad \Rightarrow \quad \Phi(x) = \left(\left(\frac{3}{4}(x+d)\right)^4\left(\frac{j_\mathrm{i}}{\varepsilon_0}\right)^2\frac{m_\mathrm{i}}{2e}\right)^{\frac{1}{3}}. \tag{1.3}$$

At $x = -d$, both negative and positive charge density decreased to $n_\mathrm{i} = n_\mathrm{e} \approx 0.66\,\mathrm{n_{e,0}}$ (see figure 1.1), where the potential is approximately $-k_\mathrm{B}T_\mathrm{e}/2e$.
To satisfy the zero total net current condition $j_\mathrm{e} = j_\mathrm{i}$ the ions are accelerated inside the sheath towards the wall. We know from the above expression for $\Phi(x)$ that the electric field gradient towards the wall is $0 < \nabla E < \Delta\Phi$. Using the electron and ion densities one gets the following equation from this:

$$\begin{aligned} 0 > \left.\frac{\mathrm{d}f}{\mathrm{d}\Phi}\right|_{\Phi=0} &= \frac{en_\mathrm{e}\,(-d)}{\varepsilon_0}\left(\frac{e}{k_\mathrm{b}T_\mathrm{e}} - \frac{e}{m_\mathrm{i}v_\mathrm{i,0}^2}\right) \\ \Rightarrow \quad v_\mathrm{i,0} = v_\mathrm{i,B} &\geq \sqrt{\frac{k_\mathrm{B}T_\mathrm{e}}{m_\mathrm{i}}}, \end{aligned} \tag{1.4}$$

which defines the so-called Bohm criteria for $v_\mathrm{i,B}$ at the sheath edge. One can express this in terms of the *Mach number* $M = v_\mathrm{i,0}/v_\mathrm{i,B}$, where $v_\mathrm{i,B}$ denotes the *Bohm velocity*.
At the sheath edge the quasi-neutrality condition is still satisfied: $n_\mathrm{e} = n_\mathrm{i}$. The transport process in the pre-sheath is dominated by collisions with neutral gas

particles. Hence the velocity distribution function can be rewritten using the ion-neutral collisions frequency $\nu_{\mathrm{n,i}}$, which becomes

$$\frac{\mathrm{d}v_{\mathrm{i}}}{\mathrm{d}x} = \frac{\nu_{\mathrm{n,i}} v_{\mathrm{i}}^2}{v_{\mathrm{B}}^2 - v_{\mathrm{i}}^2} \quad . \tag{1.5}$$

From equation 1.5 we can see: ions with velocities smaller than the Bohm velocity are accelerated inside the pre-sheath to Mach equal one or greater according to equation 1.4:

$$M \geq 1 \Leftrightarrow v_{\mathrm{i}}(-d) \geq v_{\mathrm{B}} \, . \tag{1.6}$$

1.2 Sheath Effects in RF Discharges

In my thesis I am interested in asymmetric, capacitively coupled radio frequency plasmas. In the following sections I want to highlight the most important aspects of ccrf discharges for my work. A more in-depth approach can be found in, e.g. [18].

The rf plasmas studied here are driven at a frequency of 13.56 MHz. The modulation of the potential at the electrode within one rf cycle leads to time-dependent plasma properties. Because of $\omega_{\mathrm{p,i+}} < \omega_{\mathrm{p,i-}} < \omega_{\mathrm{rf}} \ll \omega_{\mathrm{p,e}}$ all plasma species interact with the rf voltage differently. The electrons follow the applied field instantaneously, where as the ions can be considered stationary. The modulation of the electron density to the rf induces also sheath oscillations of the electrons with the same frequency. A scheme of the plasma pre-/sheath can be seen in figure 1.1.

Usually, ccrf plasmas have asymmetric characteristics. The asymmetry is created by the different areas of driven electrode and grounded walls. For example, let us assume that only the cathode is driven with rf, and that anode and plasma chamber are grounded resulting in a much larger area of the grounded part compared with the driven electrode area. The sheath then develops like explained above.

If the cathode is capacitively coupled to the driver, there can not be any net current over one rf cycle. The accumulated charge on the electrode can not be flushed and the *self bias* establishes to satisfy continuity $j_{\mathrm{e}} = j_{\mathrm{i}}$. The capacitance can not be inverted over the course of one rf cycle. The electron currents are then equal on both electrodes, therefore shifting the minimum plasma potential to ground and the maximum to the excitation. The dc *self bias* part U_{sb} and the mean plasma potential $\overline{\Phi_{\mathrm{p}}}$ becomes:

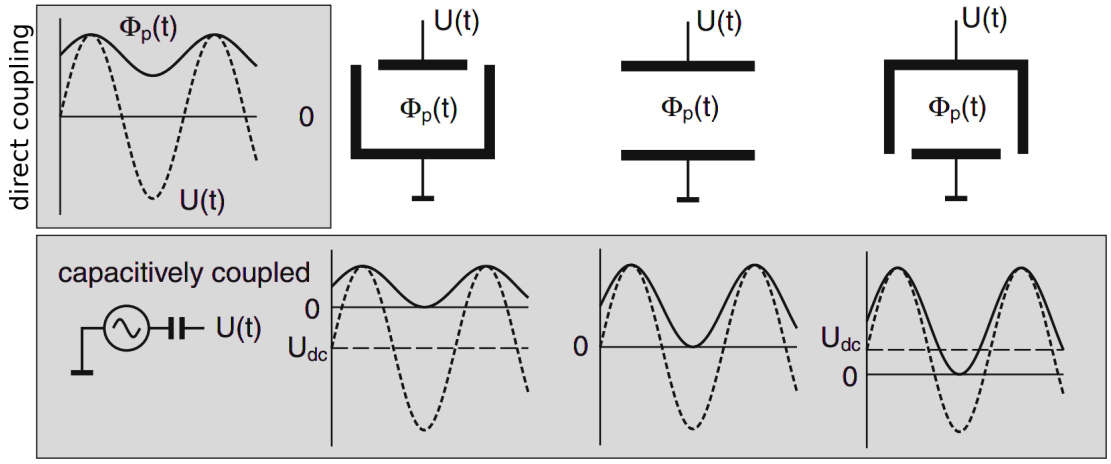

Figure 1.2: Schematics of the voltage $U(t)$ and plasma potential $\Phi(t)$ for a directly and capacitively coupled rf discharge. Different cases of symmetry are shown: enlarged driven electron, grounded electrode and a symmetric discharge. [18]

$$\overline{\Phi_\mathrm{p}} = \frac{1}{2}(U_\mathrm{sb} + U_\mathrm{rf}) \quad \text{and} \quad U_\mathrm{sb} = \frac{C_1 - C_2}{C_1 + C_2} U_\mathrm{rf}\,, \tag{1.7}$$

where $C_{1,2} = \varepsilon_\mathrm{p}\varepsilon_0 \frac{A}{b}$ are the capacities of the corresponding plasma sheath. Here, A and b are cross section and thickness of the space charge volume, and ε_p denotes the permeability of the working gas. Hence the value of the self bias becomes a function of discharge geometry, working gas and plasma sheath. For example, larger ratios of asymmetry, e.g. $C_1 \gg C_2$ lead to large values of U_sb. A common approximation for the self bias voltage is roughly half of the driven electrodes peak-to-peak voltage: $|U_\mathrm{sb}| \approx U_\mathrm{rf}/2$.

Figure 1.2 shows a scheme for different kinds of asymmetric setups, e.g larger electrode or grounded wall sizes. The corresponding plasma potential and self bias voltage for a capacitive coupling are displayed below. One can see that the self bias heavily depends on the kind of asymmetry in the ccrf discharge.

Both sheaths of the electrodes collapse completely during a full cycle of $U(t)$. At this moment, no potential barrier or space charge is hindering the particles to hit the electrodes. Electrons and ions can impinge on the surface and force the plasma potential Φ_P to level out with the walls. This short circuit between plasma and sheath occurs when Φ_P becomes negative with regard to the excitation:

$$\Phi_\mathrm{p,max} = \overline{\Phi_\mathrm{p}} + \Phi_\mathrm{rf} \geq U_\mathrm{sb} + U_\mathrm{rf}\,, \qquad \Phi_\mathrm{p,min} = \overline{\Phi_\mathrm{p}} - \Phi_\mathrm{rf} \geq 0 \tag{1.8}$$

If there is no special coupling between electrode and electrical driver, the equality in equation 1.8 is true.

1.3 Heating Mechanisms

Ohmic Heating In a spatially uniform electric field that oscillates harmonically perpendicular to the electrodes, as it is the case in the bulk of a rf plasma, charged particles periodically gain and lose energy in the absence of collisions without any net energy gain [20]. This is due to the symmetrical de-/acceleration in the sheaths over one rf cycle. Let us assume the electric field to have no or a negligible component parallel to the electrodes. Hence the mean absorbed power by the charged particles in an oscillating electric field is

$$\overline{P}_{\mathrm{ohm}} = \omega_{\mathrm{rf}} \int_0^{T_{\mathrm{rf}}} j_{\mathrm{tot}}(t) \cdot E(t) \mathrm{d}t \,, \tag{1.9}$$

where j_{tot} is the total charge current density. The total mean power dissipated into the charged species through acceleration and neutral gas friction becomes

$$\overline{P}_{\mathrm{ohm}} = \frac{|E_0|^2 \,\mathrm{Re}(\sigma_{\mathrm{p}})}{2} \approx \frac{m_{\mathrm{e}} \nu_{\mathrm{n,e}} l}{2 e^2 n_{\mathrm{e}}} j_0^2 \,, \qquad \sigma_{\mathrm{p}} \cong \frac{n_{\mathrm{e}} e^2}{m_{\mathrm{e}} (\nu_{\mathrm{n,e}} + \mathbf{i}\omega_{\mathrm{p}})} \,. \tag{1.10}$$

Here, σ_{p} is the plasma conductivity, which yields $j_0 = \sigma_{\mathrm{p}} E$, and l the bulk length. This demonstrates that power from an spatially uniform, harmonically oscillating electric field can only be transferred via collisions — the power is zero, if collisions are zero.

Elastic charged-neutral collisions transfer energy into a direction perpendicular to the field. This component is not lost during the reversal of $E(t)$. Therefore

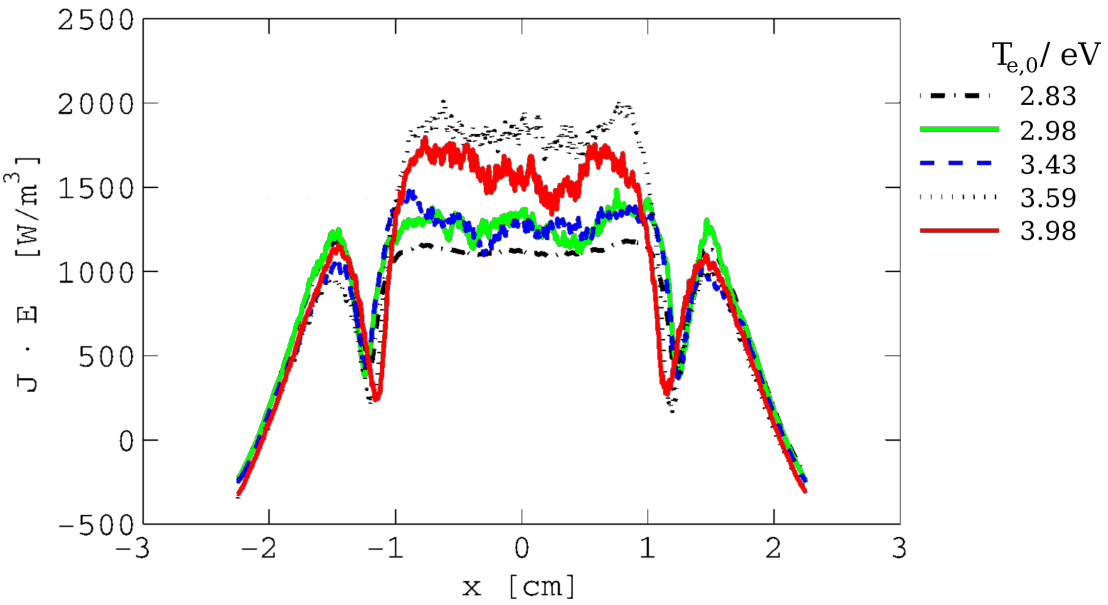

Figure 1.3: Electron heating rate for a ccrf discharge of parallel plates at 6.7 Pa with an electrode gap of 4.5 cm at 222 V. [7]

the charged species gain energy during the field oscillation. This mechanism is called *ohmic heating* and takes place mainly in the plasma bulk.
At high pressures, e.g. $> 30\,\mathrm{Pa}$ ohmic heating is dominant due to the increased neutral gas friction and collisions. In intermediate ranges there is a mode transition to another heating process, which becomes important for lower gas pressures.

Stochastic Heating Heating mechanisms in low pressure ccrf plasmas are of particular importance, because collisions are rare and sheath processes are key to the sustainability of the discharge. Another approach on the heat dissipation in such discharges is connected to the particle acceleration inside the plasma sheath. Here, collisionless energy gain in the sinusoidal modulated space charge in front of a wall is assumed. A 'hard wall' approximation (HWA) is made, where the charged particles are considered to collide elastically with the oscillating sheath edge. Heating power is then averaged by reverse and forward energy fluxes into and out of the sheath respectively. This process, though relying on enough randomisation in phase-space inside the bulk, sufficiently creates a net heating of the plasma [6, 5]. This is referred to as *stochastic heating*. The parameter K defines the degree of randomisation:

$$K = \alpha\,\beta\,\frac{U_{\mathrm{sb}}}{\epsilon E} \quad \Leftrightarrow \quad E < m_{\mathrm{e}}\,\omega^2 s_0\,l\,\frac{U_{\mathrm{rf}}}{U_{\mathrm{sb}}}\,. \tag{1.11}$$

It is derived as a measure of phase-space chaos by electron movement. Chaotic motion occurs in this mapping for $K > 1$ [5]. It decreases with increasing energy, so the system is less stochastic at higher energies. Phase correlations between successive collisions in and with the plasma sheath are reduced at higher energies, and thus decrease stochasticity.
One can calculate the instantaneous power dissipated into the plasma due to this heating mechanism. Here, using the sheath speed u_{s}, the electron drift velocity u_{e} and the Maxwell electron velocity distribution function $f_{\mathrm{v}}(v_{\mathrm{e}}, t)$, according Lieberman [10] one can find

$$P_{\mathrm{stoc}}(t) = -2m_{\mathrm{e}} \int_{u_{\mathrm{s}}}^{\mathrm{inf}} u_{\mathrm{s}}(v_{\mathrm{e}} - u_{\mathrm{s}})^2\, f_{\mathrm{v}}(v_{\mathrm{e}}, t)\mathrm{d}v \;\approx\; \frac{m_{\mathrm{e}} u_{\mathrm{e}}}{2e^2 n_{\mathrm{e}}} j_0^2\,. \tag{1.12}$$

At low pressure, e.g $< 10\,\mathrm{Pa}$, stochastic heating is the most important energy dissipation process [4, 3]. Figure 1.3 the net electron heating rate at given bulk temperatures is shown. Inside the bulk, a plateau can be seen which originates from the stronger ohmic heating in the discharges main volume. Towards the edges of the plasma around +/-1.5 cm larger peaks in the heating rate build up due to the stochastic heating at the sheath edges. For certain parameters both

mechanisms may yield a comparable net heating. Due to significant deviations of the model from the real physics in the HWA [7, 10], ohmic heating might be considered a more reliable assumption as the plasmas main heat generation process. The fundamental plasma physics needed for this thesis has now been

introduced. Further details can be found in [18, 20, 16]. To get an insight into the microscopic processes in a ccrf discharge I will use a kinetic Particle-in-Cell simulation. A kinetic model is needed to be able to resolve the distribution functions properly, which is required to be able to answer my second research question, namely the influence of surface effects on the distribution functions of negatively charged oxygen ions measured at the grounded electrode. Low pressure, low temperature radio frequency discharges are non-thermal plasmas with long mean free paths. Therefore, energy/velocity distribution functions are not Maxwellian and fluid models fail. A kinetic PIC code with Monte-Carlo-Collisions is used, which is introduced here.

1.4 Particle-in-Cell Simulations including Monte-Carlo-Collisions

Particle-In-Cell simulations including Monte-Carlo-Collisions (PIC-MCC) represent a powerful tool for fully kinetic plasma studies. They provide a self-consistent solution, including reaction and collision routines. They are used in all branches of plasma physics, ranging from simple laboratory discharges to electric propulsion devices, fusion plasmas and interplanetary astrophysical systems. A PIC algorithm simulates the motion of pseudo-particles in a continuous phase-space. Macro-quantities like forces, fields and densities are stored and calculated on a grid. The number of calculations needed per step to solve the equation of motion for each of the N particles sums up to $N \log(N)$, in contrast to particle-particle codes which a scale like N^2. The self-consistent electrostatic macro-fields are calculated by solving *Poisson's equation*.
In the following the basic scheme of a PIC-MCC simulation will be explained. As it was outlined by chapter 1, I will focus on the electrostatic case with $\vec{B} = 0$, as the magnetic field generated from the moving charged particles is small enough that the Lorentz force is dominated by the electric field $q_\mathrm{j}\vec{E}$.

1.4.1 Principles

In general, the spatio-temporal evolution of the velocity distribution function $f_\mathrm{j}(\vec{v},\vec{r},t)$ is given by the *Boltzmann equation*:

$$\frac{\partial f_\mathrm{j}}{\partial t} + \vec{v}\cdot\nabla_{\vec{r}}\, f_\mathrm{j} + \frac{q_\mathrm{j}}{m_\mathrm{j}}\vec{E}\cdot\nabla_{\vec{v}}\, f_\mathrm{j} = \left(\frac{\partial f_\mathrm{j}}{\partial t}\right)_{\mathrm{Coll}} . \tag{1.13}$$

In this equation, the product of $q_\mathrm{j}\vec{E}/m_\mathrm{j}$ denotes the electrostatic force onto the particle of species j. The velocity and space gradient are calculated like $\nabla_{\vec{r}}\, f_\mathrm{j} = \partial f_\mathrm{j}/\partial x \cdot \vec{e}_\mathrm{x} + \ldots$ and so on. The right hand side of $(\partial f_\mathrm{j}/\partial t)_{\mathrm{Coll}}$ is the sum of all collision effects on $f_\mathrm{j}(\vec{v},\vec{r},t)$. One approach would be an integral form, in which all probabilities of a two-body interactions with different incident and outgoing velocities are summed up in a convolution integral with $f_\mathrm{j}(\vec{v},\vec{r},t)$.
The approach via the distribution function yields the advantage of an easy access to the afore-mentioned macro-quantities, the zeroth and first moment are noted below in equation 1.14. Using the moments, one can write down $f_\mathrm{j}(\vec{v},\vec{r},t)$ at a thermodynamic equilibrium of $T_{\mathrm{j},0}$ as the *Maxwell-Boltzmann-distribution-function* like so:

$$n_\mathrm{j}(\vec{r},t) = q_\mathrm{j}\int_{-\infty}^{\infty} f_\mathrm{j}(\vec{v},\vec{r},t)\mathrm{d}\vec{v}\,, \qquad \langle v_\mathrm{j}(\vec{r},t)\rangle = \frac{1}{n_\mathrm{j}(\vec{r},t)}\int_{-\infty}^{\infty}\vec{v}\, f_\mathrm{j}(\vec{v},\vec{r},t)\mathrm{d}\vec{v} \tag{1.14}$$

$$f_\mathrm{j}(\vec{v},\vec{r},t) = \frac{n_\mathrm{j}(\vec{r},t)}{q_\mathrm{j}}\,\hat{f}_\mathrm{j}(\vec{v},\vec{r},t) = \frac{n_\mathrm{j}(\vec{r},t)}{q_\mathrm{j}}\left(\frac{m_\mathrm{j}}{2\pi k_\mathrm{B} T_{\mathrm{j},0}}\right)^{3/2}\exp\left(-\frac{|\vec{v}_\mathrm{j}|^2}{v_{\mathrm{j,th}}^2}\right) \tag{1.15}$$

In a Maxwellian plasma one could use a fluid approach, where the moment equations for all species are solved. This would reduce the computational cost drastically, as one would no longer have to track each particle individually, and

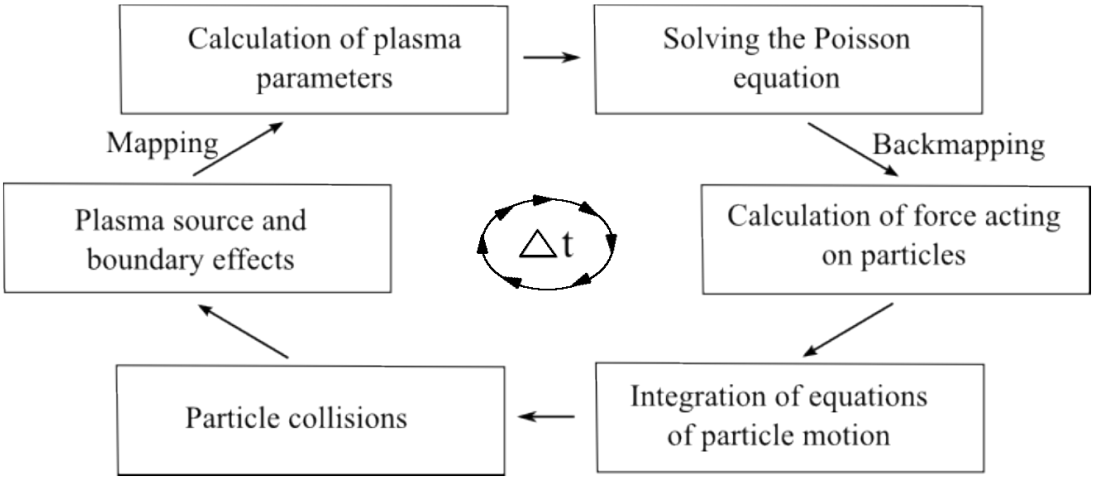

Figure 1.4: PIC simulation scheme [12].

sufficiently describe the discharge by charaterisation of macro-quantities. This is valid, if mean-free-paths are small and collisions rather likely, producing a Maxwellian distribution function. However, in a low-temperature, low-pressure ccrf discharge mean-free-paths are large and collisions are rare, which is why a fully kinetic Particle-in-Cell simulation method is used.
For a N-particle system n-th equation of motion in the N-particle system becomes:

$$\frac{\mathrm{d}\vec{x}_\mathrm{n}}{\mathrm{d}t} = \vec{v}_\mathrm{n}\,, \qquad \frac{\mathrm{d}\vec{v}_\mathrm{n}}{\mathrm{d}t} = \frac{1}{m_\mathrm{n}}\vec{F}_\mathrm{n,L}(\vec{x}_\mathrm{n},\vec{E},t) = \frac{q_\mathrm{n}}{m_\mathrm{n}}\vec{E}(\vec{x}_\mathrm{n},t) \tag{1.16}$$

where $F_\mathrm{n,L}$ is the *electrostatic Lorentz force*.
The number of N is of orders of magnitude higher than what the best supercomputers can handle. Hence it is assumed that one simulated particle at $\vec{x}_\mathrm{n}$ and velocity $\vec{v}_\mathrm{n}$ represents many physical particles. This *super-particle factor* is usually between 10^3–10^4, depending on the size and initial density in the simulated domain. Those super-particles follow the same dynamic and kinetic behaviour like their physical counterparts, because they have the same charge to mass ratio. By this, also mathematically proven, a correct solution of the kinetic equation is guaranteed.
To solve for the electrostatic force $F_\mathrm{n,L}$, the total charge density has to be calculated by interpolating the point charges q_n of each particle onto the point grid (equation 1.17). The Interpolation of particle densities to mesh points and back-mapping of the electric field to particle positions have to use the same interpolation function (usually linear) to guarantee momentum conservation.
Poisson's equation is solved globally by using the interpolated charge density on that grid (equation 1.18). This gives the the electric field:

$$\rho(\vec{r},t) = \rho(\vec{x}_1,\vec{x}_2,\ldots,\vec{x}_\mathrm{N},t)\,, \tag{1.17}$$

$$\Rightarrow \Delta\Phi(\vec{r},t) = -\frac{\rho(\vec{r},t)}{\varepsilon_0}\,, \tag{1.18}$$

$$\Rightarrow \quad \vec{E}(\vec{r},t) = -\nabla\Phi(\vec{r},t)\,. \tag{1.19}$$

A standard approach to obtain the solution of Poisson's equation is the *finite-difference method*. For a two-dimensional, with Δr equally partitioned mesh at $(r_\mathrm{l}^{(1)},r_\mathrm{m}^{(2)})$ one yields the *five point stencil*:

$$4\Phi_\mathrm{l,m} - \Phi_\mathrm{l\text{-}1,m} - \Phi_\mathrm{l+1,m} - \Phi_\mathrm{l,m\text{-}1} - \Phi_\mathrm{l,m+1} = \Delta r^2 \cdot \frac{\rho_\mathrm{l,m}}{\varepsilon_0} \tag{1.20}$$

The discrete matrix equation 1.18 is solved using a *LU-factorisation*. On the system side this process is optimised by the matrix-solver library *SuperLU* for

the direct solution of large, sparse non-symmetric systems of linear equations. There exist also other matrix-solver algorithms, for example the successive-over-relaxation (SOR) or gradient descent method.
The potential is calculated on every time step using this factorisation, but the latter is done only once at the beginning, because it only depends on the mesh, and hence the composition of the matrix $\Phi \in \mathbb{R}^{N_\mathrm{r} \times N_\mathrm{z}}$. At this is point any potential boundary conditions, such as external voltages $U_\mathrm{rf}(t)$ or ground $\Phi = 0$ are applied to the result of Φ.
In our simulation, the dimension of time is also represented by a grid. The stepping is done for a constant width Δt: $t \to t_\mathrm{k} = t_0 + k\,\Delta t$ (and correspondingly all other physical properties). Integrating the equations of motion at a given time step t_k from equation 1.16 is done by an energy conserving integrator scheme called Boris algorithm. It is used to calculate the new velocities and positions. To move the particle of index n and species j the following equations have to be solved at the time step k, or $k + / - \frac{1}{2}$ respectively (leap frog scheme):

$$\vec{u}_{\mathrm{n},+} = \vec{v}_{\mathrm{n,k\text{-}1/2}} + h \cdot \vec{E}_\mathrm{k}\,, \qquad h = \frac{q_\mathrm{j}}{2\,m_\mathrm{j}}$$

$$\boxed{\vec{x}_{\mathrm{n,k+1}} = \vec{x}_{\mathrm{n,k}} + \Delta t \vec{v}_{\mathrm{n,k+1/2}} \quad \text{and} \quad \vec{v}_{\mathrm{n,k\text{-}1/2}} = \vec{u}_{\mathrm{n},+} + h \cdot \vec{E}_\mathrm{k}\,,} \tag{1.21}$$

Spatial and temporal step width are crucial to the results and performance of the simulation. Due to the coupling of particle and mesh methods in the PIC algorithm, certain requirements for numerical stability have to be satisfied for the mesh size Δr and time step Δt by

$$\boxed{\Delta t_0 \leq 0.2 \cdot \omega_\mathrm{p,e} \quad \text{and} \quad \Delta r_0 \leq 0.5 \cdot \lambda_\mathrm{D,e}\,.} \tag{1.22}$$

The spatial and temporal step width should sufficiently resolve the smallest and fastest processes in the simulated model. Hence the physical scales of electron plasma frequency $\omega_\mathrm{p,e}$ and electron Debye length $\lambda_\mathrm{D,e}$ are chosen. In the PIC simulation they are used in a dimensionless form. Every other property is written the same way in relation to the electron plasma frequency and Debye length. Thus the complete algorithm becomes dimensionless. Electron bulk density and temperature are estimates for the necessary spatio-temporal resolution of the plasma and the simulated discharge equilibrates self-consistently. Therefore one has to check the results for under- or over-resolution. If the spatial partitions are made too small, e.g. the bulk density is much smaller than the estimated value, the necessary computation time rises. If vice versa non-physical behaviour might be observed in the simulation.
We will only consider the movement of charged species during the simulation.

Transport of neutrals is neglected in this work, because the distribution of the neutral gas reservoir can be considered homogeneous due to their very large mean free path of 2-30 cm, depending on the pressure. Also, because the neutral species is cold and has a very slow drift velocity — and therefore a large time scale of the transport process in the range of a couple ms — the O_2 are implemented as a stationary, inexhaustible reservoir at a constant density/pressure and temperature of $T = 300\,\mathrm{K}$. Though collision routines are still exercised, and the neutral particles do have velocity components differing from zero, the corresponding movement of the neutral species is not calculated.
Additionally an amplification factor is calculated to account for the real density of physical neutral gas particles. This is only used when collision probabilities are calculated, so that the processes with O^2 are not under-represented. It is usually between 1×10^7 , to 1×10^8 , depending on the pressure.
Because we know that the electrons are the fastest species in the discharge, and the time step is chosen to sufficiently describe all plasma processes, one can significantly save computation time when pushing the slower species less often. Therefore a subcycling routine is used, which pushes the heavier and slower ions only every few steps, e.g 2-6 code cycles. The subcycling factor is sensitive to the species velocities, because the particles should not be pushed further than one Debye length λ_D to avoid numerical problems. The subcycling method is also applied to the collision routine, which again saves more computational time. Forces acting upon the slower particles have to be summed up and average in the mean time.
After all the particles of index n are pushed according to the calculated velocity $v_{\mathrm{n,k+1/2}}$ and previous position $x_{\mathrm{n,k}}$ to their new position $x_{\mathrm{n,k+1}}$, boundary conditions such as secondary emission, reflection and absorption at walls are applied. Those processes are in general far from trivial. Therefore, a *Monte-Carlo* algorithm is used, in which a random generated number $R \in [0,1]$ is compared with the probability $P(\theta, E)$ of a corresponding physical process, e.g. secondary emission. This probability is a function of incident angle θ and energy E. For $P > R$ the secondary particle of species j is injected with a given velocity distribution $f_\mathrm{j}^{sec}(\vec{v})$, other wise the projectile is just lost (see section 1.5.3 and section 1.5).
To summarise this section, a basic simulation code cycle for one time step of a PIC-MCC method is shown in figure 1.4. More details can be found in [23].

After the PIC method has been outlined one will highlight the used collision routines and corresponding reaction set of oxygen. The importance of collisions in ccrf discharges has been discussed before in e.g. [22, 1, 7]. Furthermore, the selection of reaction sets and collisional routines respectively have been firstly

proposed by Matyash [15] for this PIC simulations. There a more in-depth approach can be found.
Because I want to investigate the negative ion dynamics, the plasma chemistry and corresponding collisions need to be discussed here. In the following paragraph and sections I will sketch the collisions and algorithms used in the PIC simulation. Therefore, an anion reaction set is firstly introduced to the two-dimensioanl PIC code.

1.4.2 Collision Routines

In contrast to a global method, which calculates every single of the N^2 particle-particle interactions, a binary collision model is used for coulomb collisions. In this algorithm only particles from the same Debye cell are considered to collide with each other. Because self-forces where excluded from the simulation by the weighting scheme in the previous section, the inter-particle forces inside grid cells are underestimated. This can partially be compensated when introducing the binary collision operator. This still satisfies energy and momentum conservation and is sufficiently accurate [23]. Random pairs of charges are chosen from one cell, so each particle has a single partner. This pair then is statistically collided using the simple approach from above of the boundary conditions. Due to the collision dynamics the full velocity triplet $\vec{v} = (v_\mathrm{r}, v_\mathrm{z}, v_\vartheta)$ needs to be resolved.
For charged-neutral collisions the classical *Monte-Carlo-Collisions* simulation method is used: let us assume the collision probability

$$P(t) = 1 - \exp(-\delta t_\mathrm{c} \cdot \nu_\mathrm{n,j})\,. \tag{1.23}$$

Here $\nu_\mathrm{n,j} = \sum_{i=1}^{I} \nu_\mathrm{n,j}^{(i)}$ is the collision frequency of neutrals and species j, written as the sum of all possible collisions. A single frequency is a function of $\nu^{(i)} = \sigma_\mathrm{i}(v_\mathrm{rel}) n_\mathrm{i}$ collision cross-section σ_i, density and relative velocity. The value of δt is the time between two successive collisions. If $\delta t = t_\mathrm{c}$ the collision time, the probability becomes $P = 1$. The minimum collision time is again given by a random generated number R

$$t_\mathrm{c}^{min} = -\frac{\ln R}{\nu_\mathrm{n,j}}\,. \tag{1.24}$$

To further reduce the computational burden, the maximum collision probability for a time step Δt is calculated by $P_{\Delta t} = 1 - \exp(-\Delta t \cdot \nu_\mathrm{n,j})$. Now it is possible to estimate the maximum number of colliding particles $N_\mathrm{Coll} = N \cdot P_{\Delta t} \ll N$. The algorithm now only has to evaluate so many potential collisions and no longer

needs to calculate the probability for each individual pair. The selection of the N_{Coll} particles is done randomly.
If the condition $R \geq P(t)$ for a particle pair is satisfied the corresponding process is executed. It is not important whether the particles are near each other in the selected Debye cell or their trajectories cross at any point. The collision routine, e.g coulomb scattering or charge exchange are carried out with no respect to particle paths or positions whatsoever.
Coulomb collisions and elastic scattering processes are treated in a centre-of-mass-system with isotropic angle distributions for χ and Ψ of random generated numbers $R_{1/2}$.

$$\Psi = 2\pi R_1\,, \qquad \chi = \sqrt{-2\langle\chi^2\rangle_{\mathrm{t}} \ln R_2}\,. \tag{1.25}$$

Afterwards the velocities are transformed back into their original form. This arbitrary collision algorithm is sufficient, because the transport processes and distribution functions are found to be the same as if a physical model would have been used [23].
For charge exchange processes the colliding particles are eventually lost and new ones created at the same location respectively, while deriving the corresponding velocities to satisfy the energy and momentum conservation.
At last, the excitation collisions are performed by an elastic scattering algorithm, which subtracts the threshold energy from the projectile before calculating the exit velocities.

1.5 Oxygen Plasma Chemistry

In comparison to most inert working gases in ccrf discharges, oxygen has a large number of reactions for collisions of elastic, inelastic and reactive collisions. Additionally, the negative ion species has to be taken into account when discussing collision processes. An in-depth benchmarking of both simulated and experimentally measured cross section data is given by Gudmundsson et al. in [7]. There, 33 collisions and reactions have been revised. In this thesis the selection of possible reactions will be based on [1] and slightly modified. The final collection of cross sections can be found in table 1.1 and are shown in figure 1.5. Those data are semi-empirical, meaning a part of them are based on measurements in finite energy ranges combined with low-/high-energy asymptotic models.
As already seen in section 1.3, collisions strongly influence the particle distribution functions and density profiles. Of high importance for plasma-assisted

Nr.	Reaction	Type
	Elastic scattering	**Energy loss**
(1)	$e^- + O_2 \rightarrow O_2 + e^-$	
(2)	$O^- + O_2 \rightarrow O_2 + O^-$	
(3)	$O_2^- + O_2 \rightarrow O_2 + O_2^-$	
	Electron energy loss scattering	**Energy loss**
(4)	$e^- + O_2 \rightarrow O_2^\nu + e^-$	Vibrational excitation ($\nu = 1, \ldots, 4$)
(5)	$e^- + O_2 \rightarrow O_2(Ryd) + e^-$	Rydberg excitation
(6)	$e^- + O_2 \rightarrow O(1D) + O(3P) + e^-$	Dissociative excitation at 8.6 eV
(7)	$e^- + O_2 \rightarrow O_2(a^1\Delta_g, b^1\Sigma_g)$	Meta-stable excitation
	Electron and ion reactions	**Creation and loss**
(8)	$e^- + O_2^+ \rightarrow 2\,O$	Dissociative recombination
(9)	$O^- + O_2^+ \rightarrow O_2 + O$	Neutralization
(10)	$e^- + O_2 \rightarrow O + O^-$	Dissociative attachment
(11)	$O^- + O_2 \rightarrow O + O_2 + e$	Direct detachment
(12)	$e^- + O_2 \rightarrow 2e^- + O_2^+$	Impact ionisation
(13)	$e^- + O^- \rightarrow O + 2e^-$	Impact detachment

Table 1.1: Most important collision and reactions in ccrf plasmas. Empirical and simulated data, which have been included in this simulation are shown in figure 1.5.

material processes is the generation of negative ions. Hence the ratio of electronegativity is very important.
I will highlight the most important collisions and reactions in the following section.

1.5.1 Collisions and Reactions

Elastic Scattering The elastic collisions of (1)–(3) conserve the particle numbers. Those are inter-species scattering processes, which will be assumed to have an isotropic inincident angle dependency [15, 1]. Intra-species elastic collisions were not very important in the selected parameter regions, though ion-ion scattering can strongly influence the IEDF at the concerned densities. When talking about elastic collision we also refer to coulomb collisions. For the electron species a binary *coulomb scattering* process was used. However, collision frequencies and therefore the corresponding mean free paths of coulomb scattering processes is large in low-temperature rf discharges. Hence they are of a minor impact.
The figure 1.5 shows the corresponding cross sections. In fact, only two are elastic processes, where as the collision of O_2^+ and the neutral molecule is a charge

exchange reaction with momentum transfer. This kind of process:

$$A^{-/+} + B \rightarrow A + B^{+/-} \tag{1.26}$$

is important for the consideration of surface effects. An ion with greater than thermal velocity coming from the wall will be cooled down by charge exchange collisions, which will transfer heat into the neutral reservoir.

Electron Energy Loss Electron energy loss occurs due to inelastic collisions (4)–(7), where an oxygen molecule is excited or dissociated into fragments. Here, the spatio-temporal evolution of the molecule or the fragments are of no interest here. Hence they are treated as test body collisions, in which only the electrons lose momentum and change direction. Again, the neutral particle reservoir is considered to equilibrate at a sufficiently short time scale $< 10^{-15}\,\mathrm{s}$. Rotational excitations are found to be unimportant, though the vibrational parts considerably influence the EEDF [7]. The isotropic post-collision relative velocity change in the centre-of-mass system gives

$$\widetilde{v}_{\mathrm{rel}} = \sqrt{v_{\mathrm{rel}}^2 - \frac{2\Delta E}{\mu_{\mathrm{i,j}}}}\,. \tag{1.27}$$

The most important electron energy loss scattering is the vibrational and electronic excitation, as well as the dissociation of the oxygen molecule.

Electron and Ion Channels The last class of collisions concerned here are the electron and ion production processes. Collisions (8) and (9) are the annihilation of the two oppositely charged particles, namely recombination processes. The ion-ion neutralization is constructed by a *Landau-Zener* model [17], where the adiabatic energy of the (O^-,O_2^+) configuration decreases when the particles approach each other. At the critical distance R_{c} this energy drops below the one of the (O,O_2) configuration, yielding the probability to change states $\sigma_{\mathrm{r}}(E)$

$$\sigma_{\mathrm{r}}(E) = 4\pi R_{\mathrm{c}}^2 \left(1 + \frac{1}{R_{\mathrm{c}} E}\right)\,. \tag{1.28}$$

The dissociative attachment (10) and direct detachment (11) are treated as binary collisions, like the elastic electron scatter process. For the dissociative attachment from the ground state oxygen molecule a threshold energy of 4.2 eV is needed. The incident electron loses this energy to the O_2^-, which afterwards breaks up into the two fragments. The electron transition time is, again, assumed to be short on a nuclear timescale and the resulting particles share the remaining kinetic energy

of the incident electron.
In the experiment there is a second stage for the direct detachment process: through associative detachment, oxygen atom, electron and molecule form an ozone O_3 particle. This most likely due to the presence of meta-stable $O_2(a^1\Delta_g)$ [1]. After the necessary threshold energy of 1.3 eV has been supplied to directly detach O^- on an oxygen molecule, the afore-mentioned detachment takes no energy whatsoever, making it a potentially important loss channel for cold O^- ions.
For impact ionisation (12) and detachment (13) the following is assumed: first, an inelastic collision takes place, in which the electron loses the necessary reaction energy. The post-collision oxygen particle is afterwards split into an additional e^- and atom/ion (O^-/O), which proceed to perform an elastic collision. During this process, energy and momentum conservation is satisfied.

1.5.2 Anion Species

The main production channel of negative oxygen ions in ccrf discharges at low pressures and temperatures is the dissociative attachment reaction (10). Here, an electron is attached to a molecule. The successive electronic excitation is of short

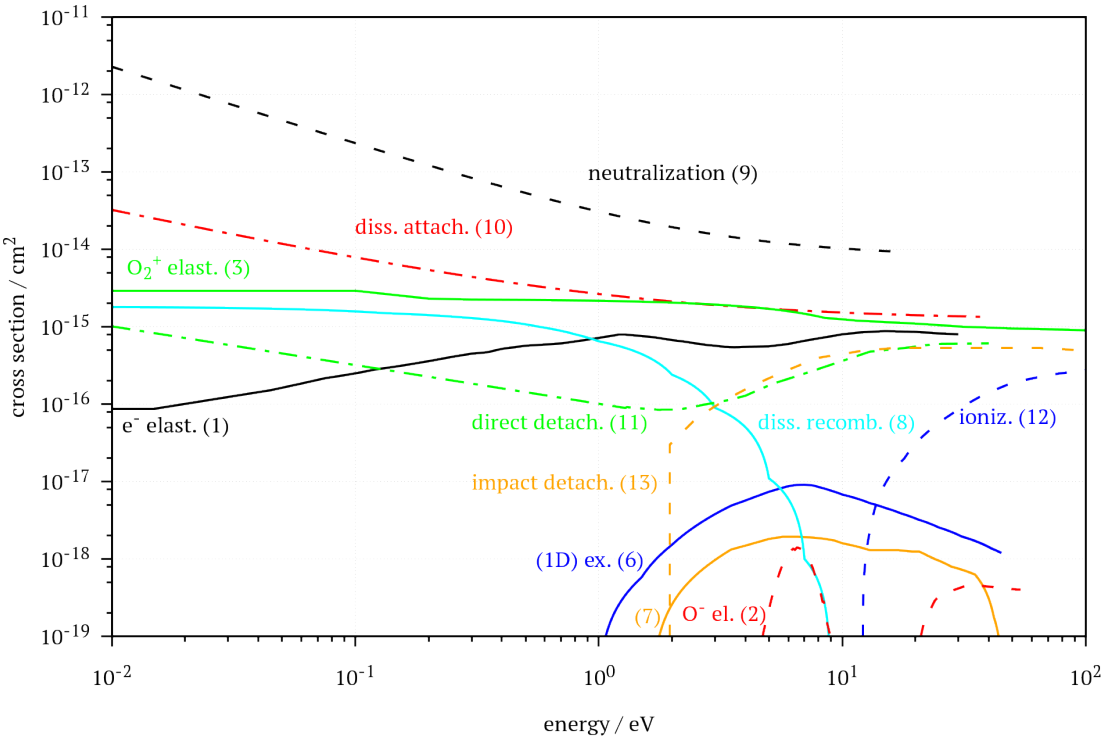

Figure 1.5: Cross section data of electron energy loss, electron and ion production/loss and elastic scattering collisions from [7] and [1]. The corresponding reaction equations are shown in table 1.1.

duration and does not change the intra-molecular distance. Afterwards, there is a significant chance of transition to a dissociative state exists, which has a lower equilibrium energy at greater intra-nuclear distances. Hence, the dissociation of this molecule is rather likely.

$$e^- + AB \rightarrow A + B^- \tag{1.29}$$

Another possible creation channel is a three-body collision of non-dissociative character, whose cross sections is magnitudes smaller than the one of equation 1.29. Hence I will only consider dissociative attachment reactions (10) for the anion production.

Negative ion loss can happen through reactions (11), (13) and (9). The latter is the only collision with a cross section larger than the creation via dissociative attachment (see figure 1.5). For all relative energies, the neutralisation has a probability of at least one order of magnitude larger than the other channels. Cross sections of direct (11) and impact (13) detachment are, depending on the energy, about one to two orders of scale smaller.

In general, the produced negative ions are cold. The anion distribution reaches until the boundaries of the bulk, where processes with large cross sections at low energies become important [1]. Those reactions would be ion-ion neutralisation and associative detachment. Direct detachment, though being still present around $E < 1\,\mathrm{eV}$, has an energy threshold and is not significant for this region. Furthermore, the probability of neutralisation (9) is proportional to the O_2^+-density. Bronold et al. [1] proposes, that the production and loss of O^- is rather insensitive to voltage changes up to 300 V. Furthermore, the most important range for incident energies will be 4–15 eV, while the EEDF is rather voltage-independent.

Considering the physics of a negative ion — O^- follows the same dynamic and kinetic behaviour as the electrons, but is easily confined by the plasma potential due to their much greater mass and, hence $\omega_{\mathrm{p,i\text{-}}} << \omega_{\mathrm{p,e}}$ — the main loss and production channels are most prominent in the bulk. Therefore, a low-pressure, low-temperature ccrf discharge has an electronegative core, in which the cold anions are captured, and areas where they are excluded. The presence of negative ions also has a great impact on the distribution functions of other plasma species. It is possible to form a quasi-neutral volume core, consisting only of ion species, and a peripheral electron-ion plasma in the discharge sheaths [22]. At pressures $> 30\,\mathrm{Pa}$ and large input powers, the value of electronegativity α leads to instabilities between ionisation and electron attachment reactions. The electron density peaks as the corresponding temperatures drops. Because of the strong negative

ion coupling, the O^- density fluctuates as well.

1.5.3 Surface Effects

Although the sheath physics are influenced by plasma properties in front of the wall, such as temperatures and densities, they are also sensitive to wall processes. One important aspect is the absorption and re-emission of charged species. In my thesis I am only interested in surface processes of negative ions and their effect on the EDF.

Experimental results from [19] and [9] indicate that ions are produced near the surface of a metal electrode and heavily accelerated in the plasma sheath. In theory, secondary emission by surface ionisation — in analogy to the surface neutralisation — occurs with incident atoms of thermal energy. Hence one assumes a positively biased wall at high temperatures as the target. Its valence level is therefore broadened, giving an atom A the chance to deposit an electron at the metal and be emitted as an ion A^+.

This statistical process can be described by a thermodynamic equation (see equation 1.30) yielding the ionisation coefficient of A. In equation 1.30 a modified approach for the *Saha-Langmuir equation* on the degree of ionisation in gases can be found. Here, the surface temperature T and average work function $\overline{\Phi}_+$ are important quantities. Additionally, the ionisation energy $I(A)$ — or impact energy —, the particle fluxes of both species j and j^+, corresponding statistical weights w, w^+ and reflection coefficients at the intrinsic potential barrier r/r^r are used.

$$A \leftrightharpoons A^+ + e^-$$
$$\alpha^+(A^+) = \frac{j^+}{j} = \frac{(1-r^+)\,w^+}{(1-r)\,w} \cdot \exp\left(\frac{\overline{\Phi}_+ + e\sqrt{eV_{\text{ext}}} - I(A)}{k_{\text{B}}T}\right) \tag{1.30}$$

The Schottky term $e\sqrt{eV_{\text{ext}}}$ describes the reduction of the work function of electrons in a metal solid due to a large external electric field. At high temperatures of, e.g. 1000 K and applied voltages $V_{\text{ext}} < 1\,\text{kV}$, this term and the corresponding internal reflection coefficients r/r^+ can be neglected — it appears to be just half of the thermal energy at room temperature. However, theoretical studies for such coefficients are missing.

In addition to SIE of positive ions, the model can be easily applied for negative ions with small changes to equation 1.30: a negatively biased electrode is assumed and the average work function yields a different sign. The electron affinity of the

incident particle B is $A(B)$.

$$B + e^- \leftrightharpoons B^-$$

$$\alpha^-(B^-) = \frac{(1-r^-)\,w^-}{(1-r)\,w} \cdot \exp\left(\frac{-\overline{\Phi}_- + e\sqrt{eV_{\text{ext}}} + A(B)}{k_{\text{B}}T}\right) \tag{1.31}$$

Applying the former assumptions to both equations of positive and negative ions, inserting a homogeneous work function $\Phi = \overline{\Phi}_- = \overline{\Phi}_+$ for the used substrate yields the originally derived *Saha-Langmuir equations*:

$$\alpha^+(A^+) = \frac{w^+}{w}\,\exp\left(\frac{\Phi - I(A)}{k_{\text{B}}T}\right), \qquad \alpha^-(B^-) = \frac{w^-}{w}\,\exp\left(\frac{-\Phi + A(B)}{k_{\text{B}}T}\right). \tag{1.32}$$

Though only considering atomic particles onto the wall, forms similar to equation 1.32 can also be derived for molecular surface interactions [8]. For conditions and materials of ccrf discharges no calculated reflection coefficients exist.
Works of, e.g. [24] and [11] investigated ion beam scattering, electron loss and transport in plasma sheath environments for metal walls, especially MgO(100) surfaces. There Ustaze et al. [24] studied incident oxygen gas particles — ions and neutrals — on magnesium oxide surfaces. Impinging atoms became negatively charged ions, picking up electrons from the MgO of the wall. This interaction, though requiring a minimum ionisation and seperation energy for the electron, is most effective at low energies $< 1\,\text{eV}$. This is due to a maximum of residence time at the target for an incoming atom. Hence it can be considered a non-resonant charge transfer process at the anion site. Further details can be found in [8].

Chapter 2

Experiment

The experiment by Scheuer et al. [19] is used for this study. It consists of a cylindrical stainless steel vacuum chamber, filled with oxygen at low pressures and gas flow rates (see figure 2.1). It has a diameter and height of 40 cm respectively and was filled with the process gas oxygen (O_2) at 5 sccm (**FC**). The discharge configuration consists of an electrode in the centre with 10 cm of diameter and a rf generator, constantly operating at a frequency of 13,56 MHz and power outputs between 5 and 150 W (**RF** and **AN**), leading to applied voltages in the range of 100–1500 V. The electrode gap was about 5 cm. Shielding and discharge enclosure/chamber walls are grounded. This results in a large area

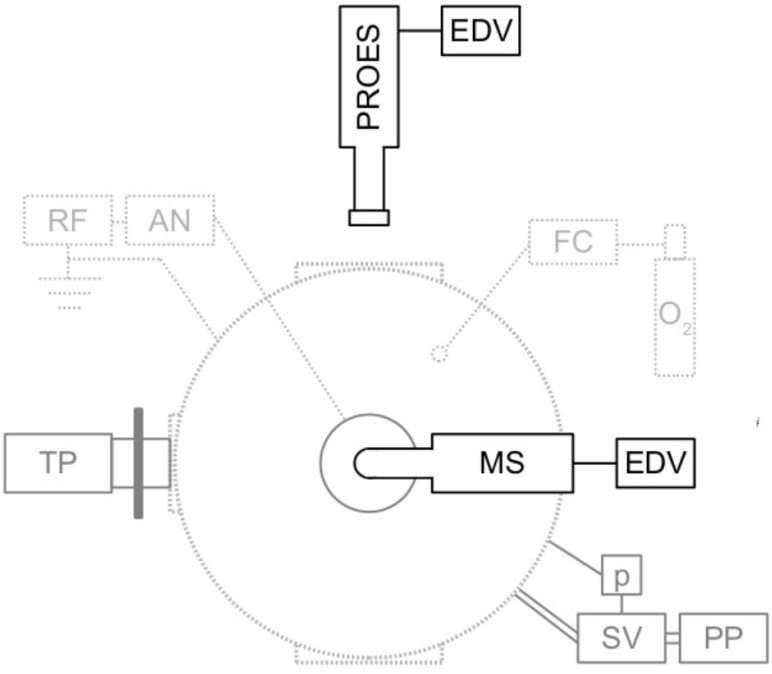

Figure 2.1: Top-down view schematic of the experiment [19], [9]. Shown is the setup without microwave interferometer, like it was used by Küllig et al.

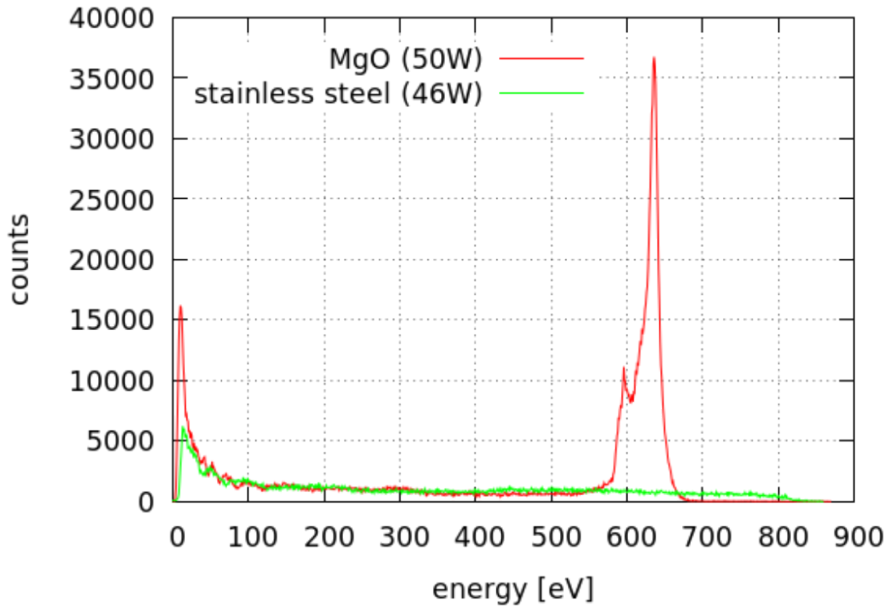

Figure 2.2: Positive and negative ion energy distribution functions at different cathode power outputs and materials. [19]

ratio between grounded and driven electrode producing an asymmetric plasma. The powered electrode was coupled capacitively with the external generator. The self bias voltage U_{sb} ranged, depending on power output and discharge pressure, from -100 up to 500 V. In [9] the experiment was pulsed with short discharges at a frequency of 10 Hz. Line integrated measurements of average electron density gave 10^{11}–$10^{12}\,\mathrm{cm}^{-3}$. Showing a schematic top-down view of the experiment is figure 2.1. Here, the large ratio between driven and grounded parts is easily recognised.

The figure includes further diagnostics like a mass spectrometer (**MS**) and phase resolved optical emission spectroscopy (**PROES**). The latter measured the densities via line integration across the plasma volume. The MS is a key instrument for the investigation pursued in this thesis, as it also measures particle numbers energy resolved. For example, the ions created via secondary processes in the discharge sheath are accelerated towards the bulk and thus get into the MS with their characteristic speeds and mass. A significant increase of electron density was found for rf powers larger than 50 W or -220 V self bias voltage [9]. This led to a correlating negative oxygen ion density reduction and decrease of the electronegativity ratio $n_{i,-}/n_{\mathrm{e}}$ from 4 to 0.03. During a different operation mode — called α-mode, contrary to the afore-mentioned γ-mode — at less than 50 W output power, electronegativity rises again, as well as the electron temperature T_{e}, yielding higher rate coefficients for, e.g. dissociative electron attachment and the alike.

Experimental results of positive and negative ion distribution function measured

by the mass spectrometer are shown in figure 2.2. The numbers of O^- detected on the anode is much lower than those of O_2^+. Both distribution functions show a low energy peak and a following plateau up to several hundred eV. For the positive ion EDF there is a peak at around 15 eV to 20 eV, depending on the material and input power. For MgO only we can find a large number of high energy, namely 600 eV to 700 eV, negative ions at the anode.

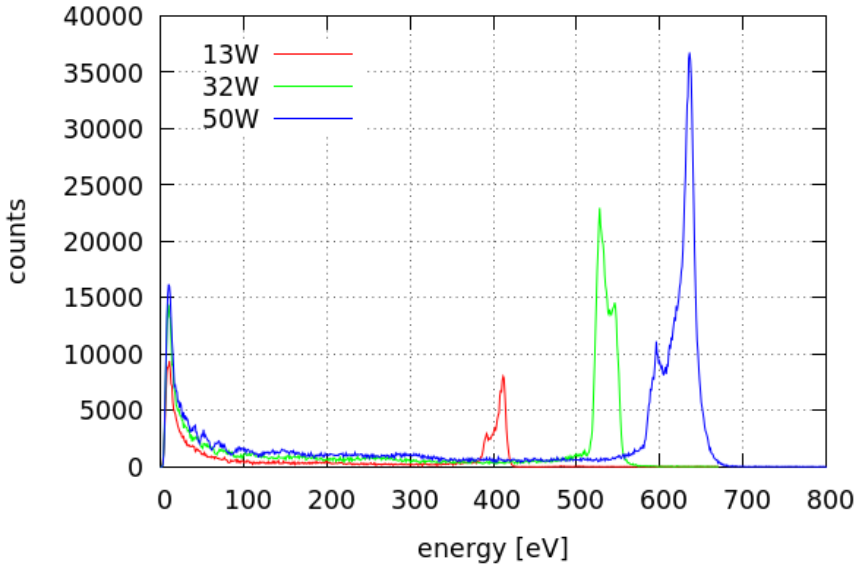

Figure 2.3: Energy distribution of negative ions O^-. Experimental results for MgO measured at the anode for different rf powers.

Chapter 3

Results of 1d3v PIC Simulation

An existing 1d3v Particle-in-Cell code [14, 13, 1] is used to understand the fundamental physics in a ccrf discharge of low pressures of oxygen. The limits of the code with respect to a realistic description of the experiment will also be discussed, which can only be resolved with a two-dimensional simulation.

3.1 Low Pressure Discharge of Oxygen

The 1D PIC-MCC code is applied to oxygen plasmas. Cross-section data for collisions are used as presented before in section 1.5.1 and shown in figure 1.5.
The simulation model resembles a parallel plate rf discharge. The electrodes are placed at both ends of the domain, e.g. $x = 0$ and $x = N_z \cdot \Delta z_0$. Scaling parameters were chosen as $n_{e,0}$ =$5 \times 10^9\,\mathrm{cm}^{-3}$ and $T_{e,0}$ =5 eV. This results in a Debye length $\lambda_{D,e} = 0.0234\,\mathrm{cm}$ and an electron plasma frequency $\omega_{p,e} = 3.98 \times 10^9\,\mathrm{Hz}$. The size of a cell is $\Delta z_0 = 0.0117\,\mathrm{cm}$.
The domain length was set to $N_z = 426$ cells, which corresponds to 5.0 cm. Experience has shown that too small simulation domains result in a too small plasma bulk [12], contradicting experimental observations. In such a case, the discharge would be dominated by the space charge sheaths in front of the electrodes. Therefore, no sufficiently sized plasma can be established to investigate the important ion dynamics. Parameters chosen here guarantee sufficiently large bulk regions.
The cathode is driven sinusoidal at a frequency of 13.56 MHz with a voltage amplitude of 400 V. It is placed at z =5.0 cm. The proposed model from section 1.5.3 for the injection of negative ions at a surface is implemented and used here. An injection efficiency of $\eta = 0.03$. [16] is used due to the lack of reliable data.

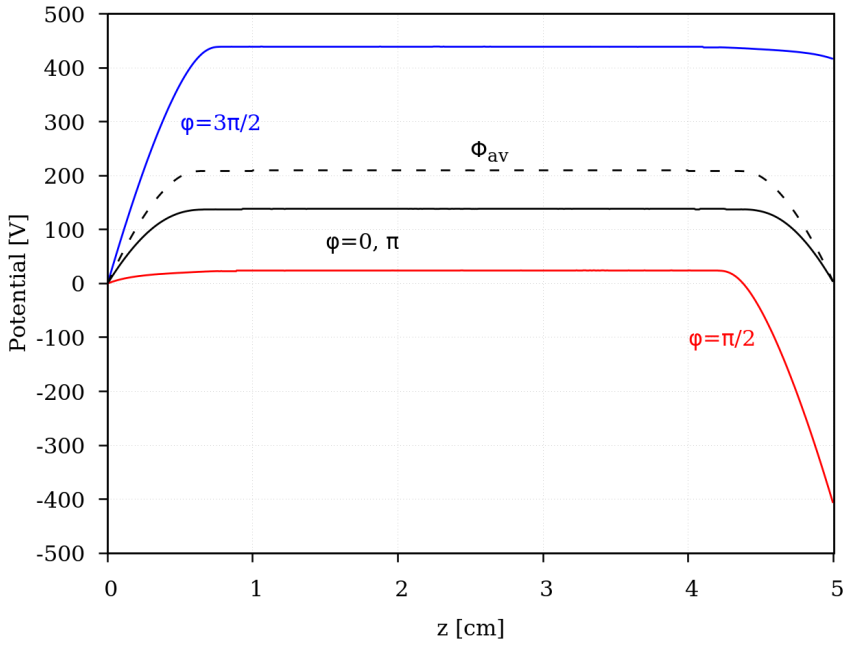

Figure 3.1: Phase resolved potential. Dynamics of the potential for U_{rf} =400 V during one rf cycle, with the mean plasma potential Φ_{av}.

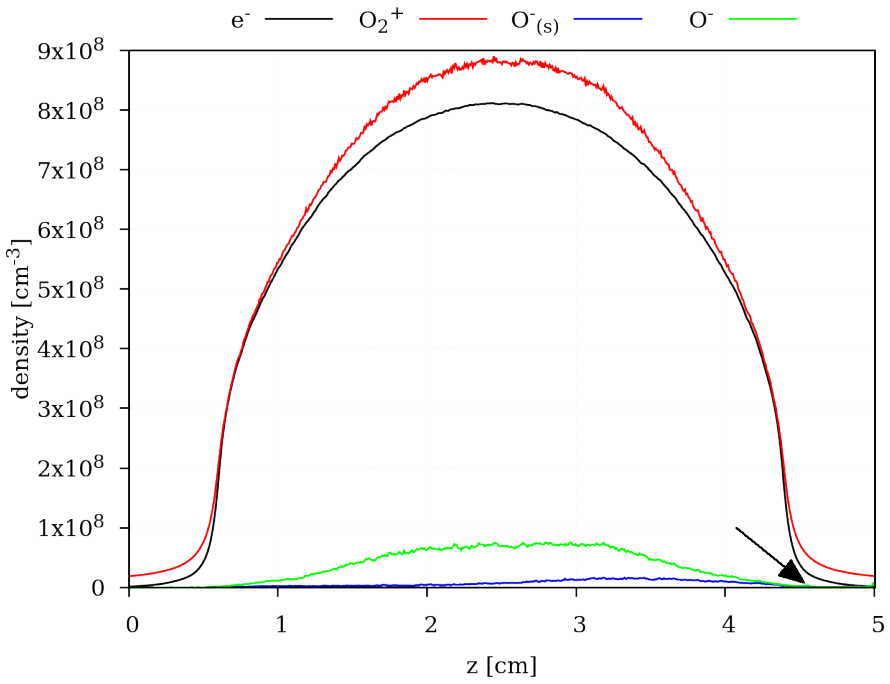

Figure 3.2: Density distribution of electrons, postive and and negative ions. The density of negative ions produced by surface processes was separated.

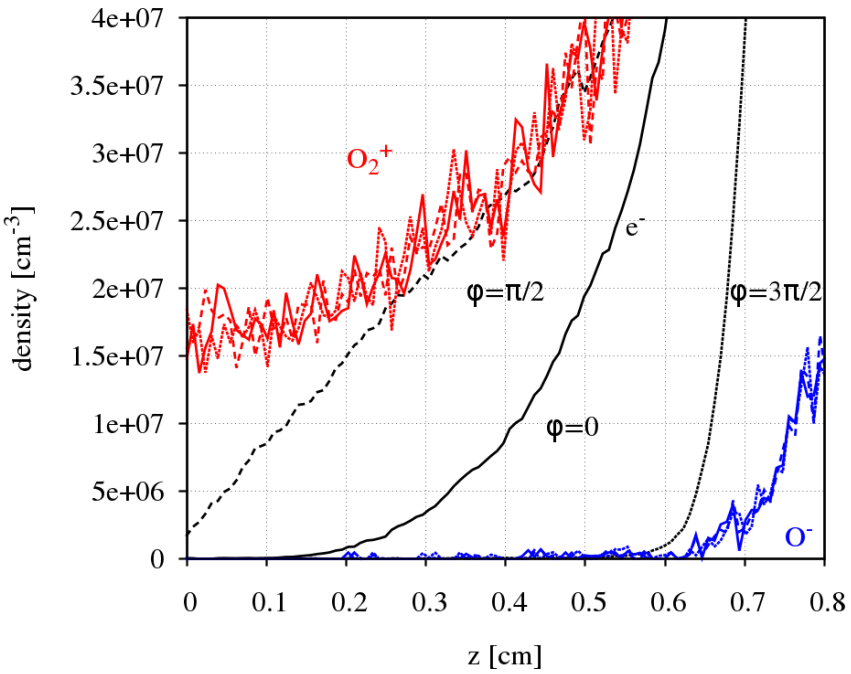

Figure 3.3: Phase resolved density of electrons, positive and negative ions at 2 Pa and 400 V. Dashed and dotted lines are at different phases for all species, respectively.

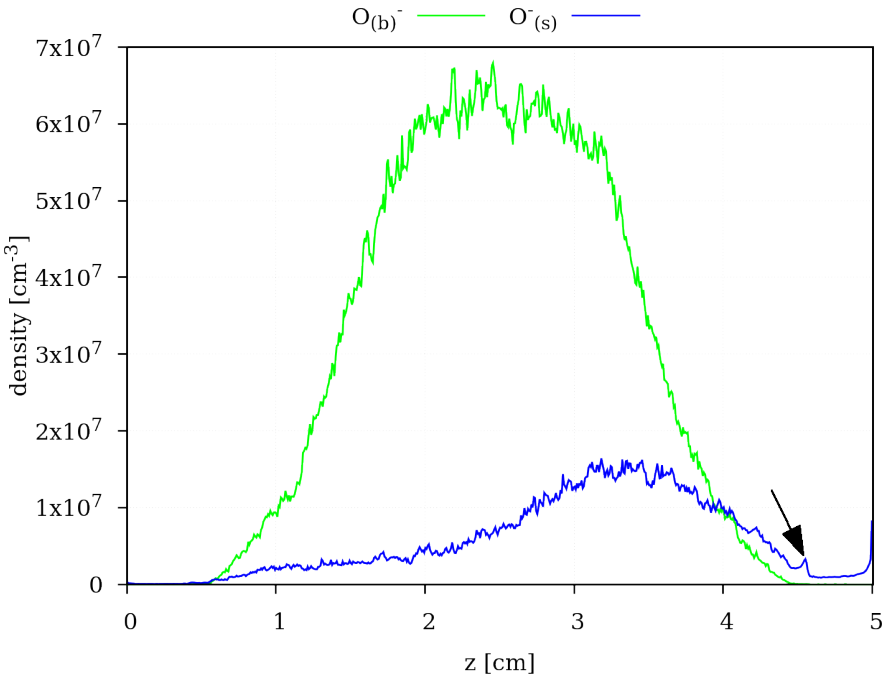

Figure 3.4: Density of negative ions that have been produced in the bulk and at the surface — subscript (b) and (s) respectively.

Initially, all particles are randomly distributed across the whole domain. This includes the same amount of electrons and ions. The initialisation of a plasma bulk reduces the start-up in comparison to the initialisation of only a small number of free electrons and subsequent build-up of the rf plasma. The neutral gas is treated with $n_\mathrm{n} = const.$ as an inexhaustible reservoir with fixed temperature $T = 300\,\mathrm{K}$. The neutral pressure was chosen between 2–10 Pa.
Potential, ion and electron densities are shown in figure 3.1 and figure 3.2. The potential is shown for different phases of the rf pulse. Also, the time-averaged plasma potential Φ_av is presented. Though the plasma potential is dominated by the driver on a shorter time scale, e.g $\varphi = \pi/2, \ldots$ the mean value rests at $\Phi = 0$ at the electrodes and becomes $\Phi \approx 200\,\mathrm{V} = U_\mathrm{rf}/2$ in the bulk. The corresponding phase-resolved density distributions at the anode of electrons, negative and positive positive ions is shown next to it. One can easily see that only the electrons follow the externally applied electric field. The modulation of their density distribution is namely the oscillation of the space charge sheath, because both ion species remain stationary throughout the rf cycle.
Figure 3.2 underlines the findings from figure 3.1. The charged species form a well developed plasma bulk of approximately 3.5 cm length. Plasma sheaths on both sides are equally spaced with $0.75\,\mathrm{cm} \sim 32 \cdot \lambda_\mathrm{D,e}$. They build up due to the potential drop between plasma bulk and electrodes. Because of the results from equation 1.3 by Langmuir we know that the sheaths potential is a function of the unperturbed ion plasma current, or vice versa. Hence, the sheaths thickness establishes self consistently to satisfy current continuity $j_\mathrm{e} = j_\mathrm{i}$ at the boundaries. One also finds the electron density to decay much faster towards the walls in comparison the positive and negative ions. This is in agreement with the one-dimensional approximations from equation 1.2, where electron numbers decrease exponentially and the ion density only descends to the power of $-1/2$. Additionally, the potential drop between bulk and electrodes is equal on both sides, even when only one electrode is driven. It builds up self-consistently due to the afore-mentioned different ion and electron dynamics.
In figure 3.2 one can see that the sum of negative ion and electron density equals the positive ion density in the bulk due to the quasi-neutrality constraint. Towards the electrodes the plasma space charge separation establish and sheaths form as discussed before in section 1.1.The density of negative ions produced at the surface $O^-(s)$ increases towards the cathode. This is due to their production at the electrode.
A comparison between the density of negative oxygen ions produced on the surface and plasma bulk is displayed in figure 3.4. The arrow marks a little density

peak of $O^-_{(s)}$, which was highlighted before in figure 3.2. This structure in the $O^-_{(s)}$ density is a result of the deceleration of fast particles in the bulk by energy loss collisions. They are then reflected eventually at the sheath edges because of the potential barrier at the boundary.

The total number of collisions with neutral gas molecules for negative ions from the bulk and surface is shown in figure 3.5. They include elastic scattering and charge exchange processes. As expected, most collisions happen in the bulk, but also some occur in the sheath at 5 cm. Obviously the sheath is collisional. The collisions of energetic O^- with low energy O_2 molecules at room temperature leads to a loss of kinetic energy. This is due to either elastic scattering or charge exchange processes, where the anion becomes cold when colliding with a molecule.

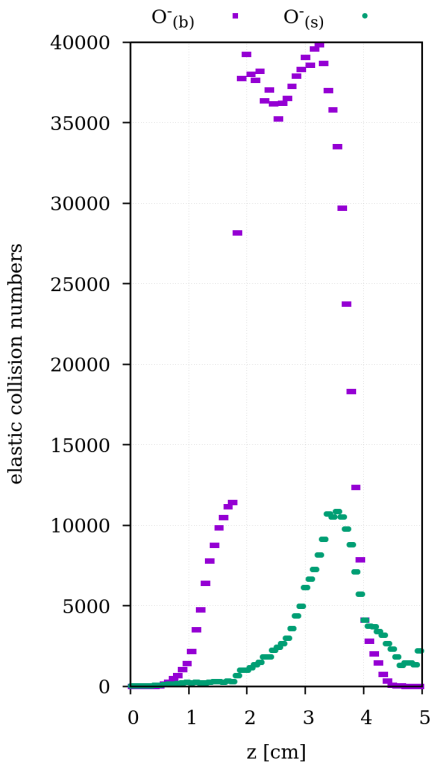

Figure 3.5: Elastic collisions of surface and bulk anions.

Because I am interested in the dynamics of the plasma the energy distribution functions of the charged species are of particular interest, especially those of the surface generated O^- ions. The next part is therefore devoted to the discussion of the particles EDF and the corresponding behaviour.

3.2 Energy Distribution Functions and Anion Dynamics

The EDFs of both ion species have large particle counts at low energy values, distributed over the plasma bulk at the centre of the discharge. The corresponding kinetic temperatures for the majority of positive and negative ions are rather low, e.g between 10^3K to 10^4K. This 'cold core' expands from 50 to 370 $\lambda_{D,e}$ and -5 eV to 5 eV respectively. The high energy part in the distribution function of O_2^+ between 0 – 50 $\lambda_{D,e}$, and 370 – 426 $\lambda_{D,e}$ is a result of the acceleration in the sheath by the potential drop of ≈ 200 V . The low energy part of the distribution establishes through energy loss collisions and bulk ionisation processes with slow

exit velocities.
There are subtle structures in the positive ion EDF between electrodes and bulk below the higher energy distribution tail. One can count 7 to 8 of such characteristic peaks on both sides. This is likely the number of rf cycles an ion stays in the plasma sheath. Assuming the ion energy is approximately 50 eV upon entering the sheath, an its thickness roughly 0.75 cm, the transit time of the incident particle is ≈ 8.3 times the duration of a full radio frequency cycle. It is de-/accelerated inside the sheath, oscillating with the phase of the external electric field. Therefore, ions can gain up to 8 times the energy from the electric field in one RF cycle while passing through the sheath and flying towards the electrode. They are eventually reflected and likewise accelerated again in the opposite direction.
The dynamics of the negatively charged electrons in the sheaths is very well highlighted in figure 3.8. One can see the acceleration between 0–50 $\lambda_{\mathrm{D,e}}$, which yields energies of up to 100 eV. The higher energy portion of the electrons from the anode traverses the bulk and is decelerated in the opposing sheath and vice versa. Also, the electron EDF has a low energy peak in the bulk between -50 eV to 50 eV, whose numbers quickly decay to higher values due to energy loss collisions.
In figure 3.9 the energy distribution of negative ions produced in the plasma bulk is shown. The form of electron and negative bulk ion EDF is similar in a sense that both show a low energy peak across the bulk length between 50 and 370 $\lambda_{\mathrm{D,e}}$. In contrast, fast electrons from the anode reach the cathode with a kinetic energy $E_{\mathrm{kin}} > 0$, as seen in figure 3.8, whereas the negative ion distribution does not have this feature. Their distribution functions shows the intrinsic de-/acceleration in the sheaths of this symmetric discharge. Anions from the bulk never gain a kinetic energy large enough to pass the potential barrier at the electrodes. They are reflected at the boundary/in the sheath and eventually make it across the bulk to be reflected again.
The distribution function of anions produced at the surface shows the acceleration by the potential drop in the plasma sheath, which yields kinetic energies up to 120 eV. The corresponding peak can be found between 370 and 426 $\lambda_{\mathrm{D,e}}$ in figure 3.9. There is also a peak at $-50\,/50$ eV between 50 and 370 $\lambda_{\mathrm{D,e}}$. This is the result of fast particles being decelerated in the plasma bulk. They are reflected at the sheath edges because of their decreased kinetic energy, and therefore do not make it to the anode. Collisionless surface ions are reflected in the opposing, which is why there are similar structures to the ones discussed earlier between 0 and 50 $\lambda_{\mathrm{D,e}}$.

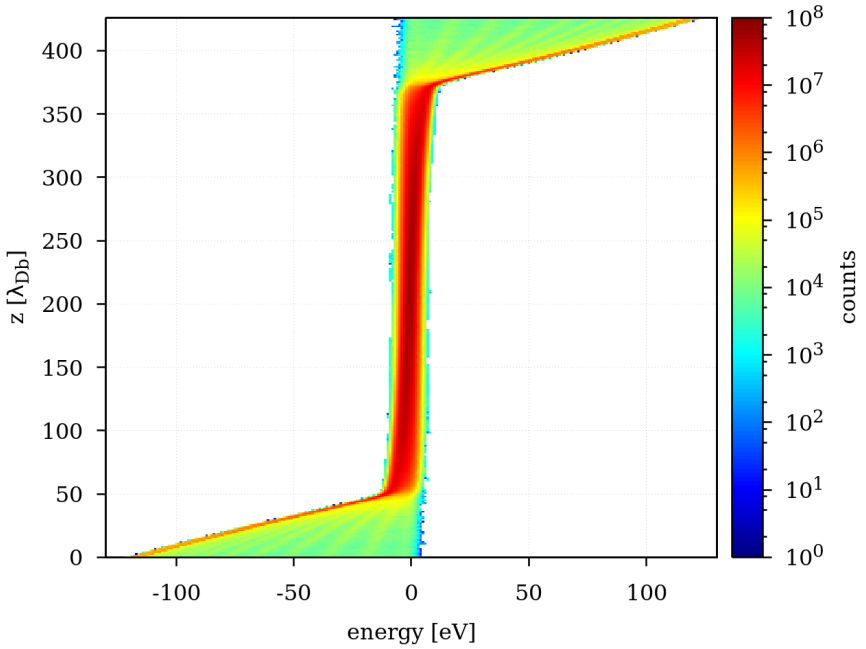

Figure 3.6: Logartihmic spatial-energetically resolved EDF of postive ions from a discharge at 5 Pa and 400 V.

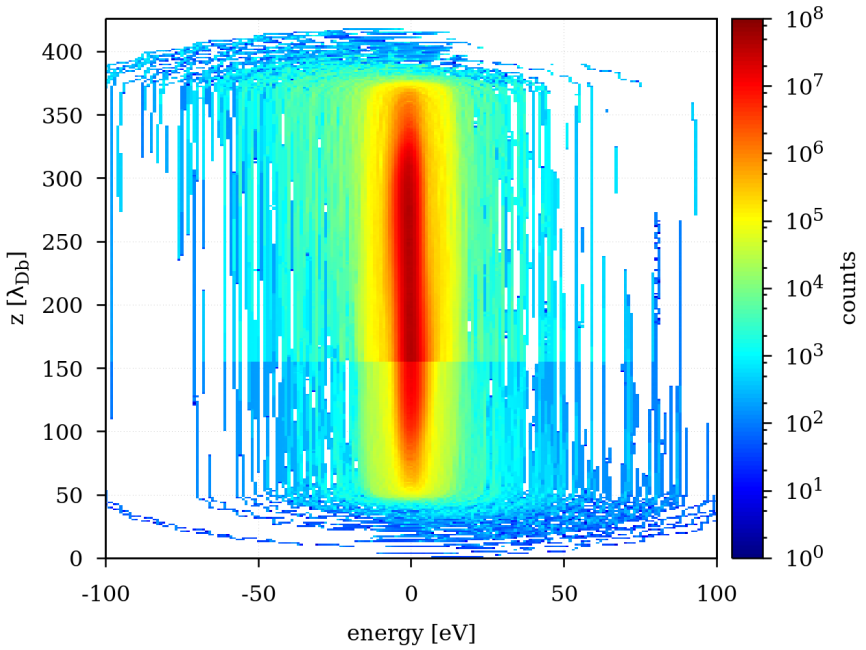

Figure 3.7: Logarithmic spatial-energetically resolved EDF of negative ions from a discharge at 2 Pa and 400 V.

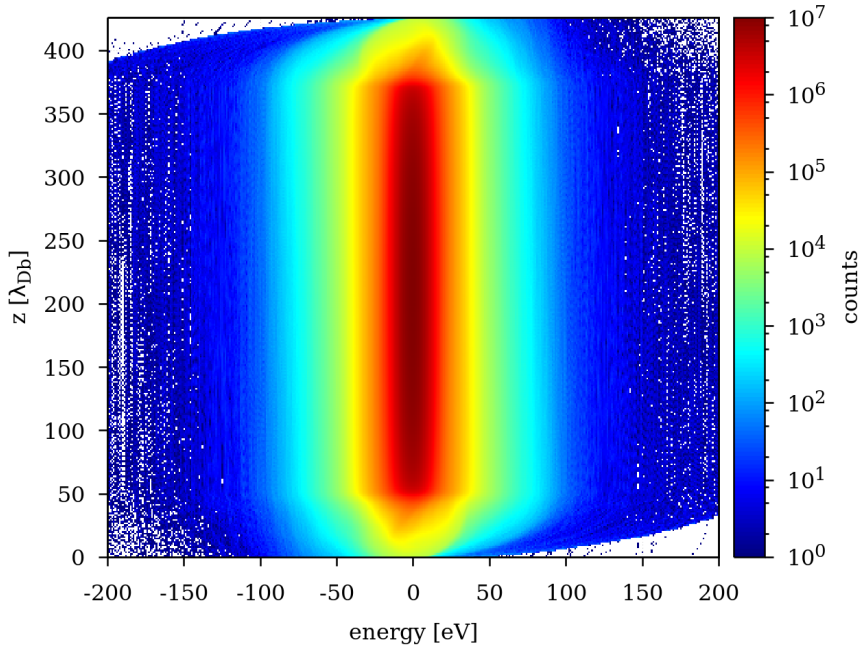

Figure 3.8: Logarithmic spatial-energetically resolved EDF of electrons from a discharge at 2 Pa and 400 V.

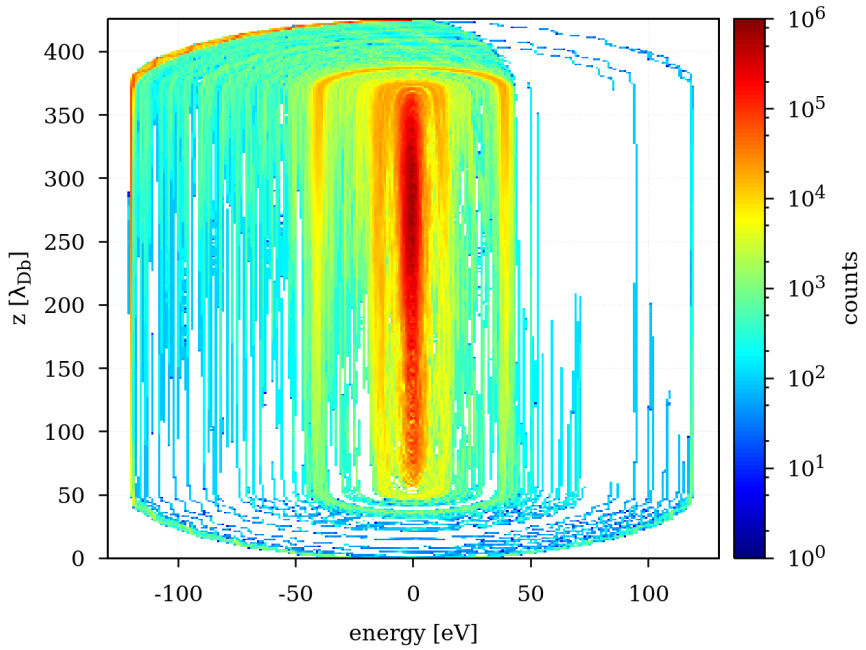

Figure 3.9: Logarithmic spatial-energetically resolved EDF negative ions produced on the surface from a discharge at 2 Pa and 400 V.

The surface anion EDF slightly increases towards the cathode. This is due to the asymmetric secondary ion emission, because we only considered the production of negative ions at the cathode. Additionally, there are also peaks similar to the one found for positive ions in the lower energy part of the EDF in front of the cathode. A closer look at this can be found in figure 3.12.
The figure 3.11 shows the high energy peak of the previously discussed surface anion distribution function. This structure decays with the mean free path of the negative ions. For example, the O^- loses energy or it is lost by detachment at O_2 and recombination with O_2^+. This also creates the density peak in front of the cathode in figure 3.4. Negative ions from surfaces may become cold through energy loss collisions, which is why they eventually remain in the bulk.
The subtle structure in the cathode sheath region of the surface anion EDF builds up due to the low transit time of a slow particle through the space charge area. Therefore the phase-resolved distribution function of the negative surface ions is shown in figure 3.12. The modulation of the electrodes and sheaths potential causes de-/acceleration of the slow particles entering at approximately 50 ev. They need 4.32×10^{-7} s to travel through a sheath of thickness 0.75 cm the given kinetic energy. It stays for roughly 5–6 rf cycles inside the sheath. This produces the same additional peak structures as for positive ions. In the phase-resolved EDF we can see anion density peaks moving according to the phase of the rf signal. Between five and six peaks are visible at a given moment in the excitation, which supports the findings from before. The ions enter the sheath easier when the voltage is positive during $\varphi \leq \pi$. Afterwards they are accelerated away from the sheath at $\pi < \varphi \leq 2\pi$. The anions/ions oscillate back and forth. Their kinetic energy is transferred into potential energy in the sheath and vice versa.
The particle numbers in the EDF of surface ions are at least one order of magnitude smaller than those of the bulk ions. This is due to the low surface production of an efficiency $\eta = 0.03$ [16] at the cathode and low pressures of 2 Pa, which favours the production of anions in the plasma volume.
Figure (3.13) confirms, in comparison with the experimental results from figure 2.2, that negative ions produced at the surface may lead to the measured high-energy peak. The energy distribution function of the simulation has additional low energy peaks at < 100 eV, too. They are created due to the energy loss by collisions and the intrinsic symmetry of the sheaths. This peak structure was also found and discussed for figure 3.11.
In the experiment all high-energy anions are detected by a mass-spectrometer and thereby removed from the discharge. In this simulation however, the collection of the energy distribution function does not perturb the results in any way.

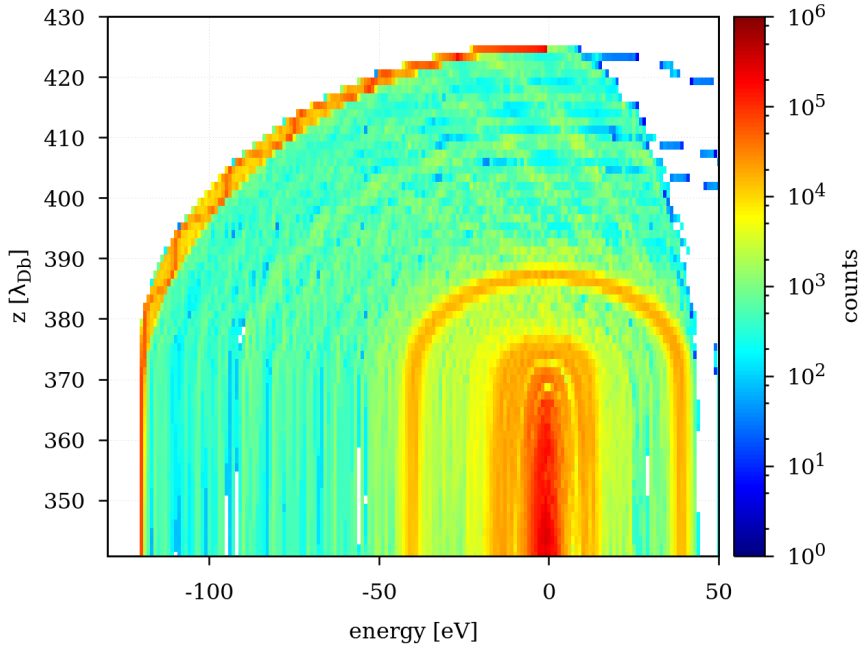

Figure 3.10: Same EDF as shown in figure 3.9. Close up the structures in the cathode sec:sheathphysics.

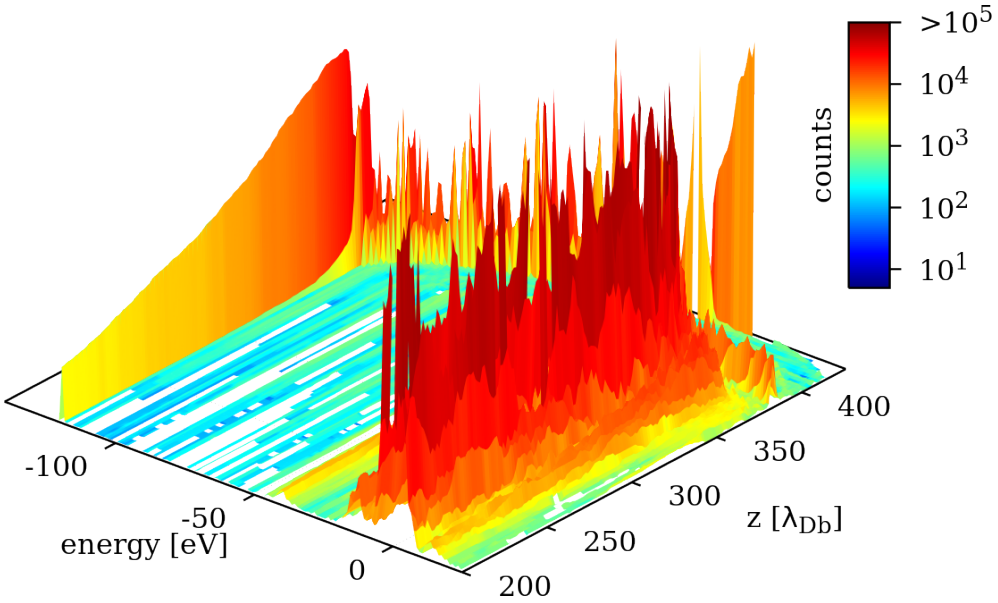

Figure 3.11: EDF as in figure 3.9 as a surface plot. One can see the energy peak at around $-100\,\mathrm{eV}$ decaying over the length of the bulk.

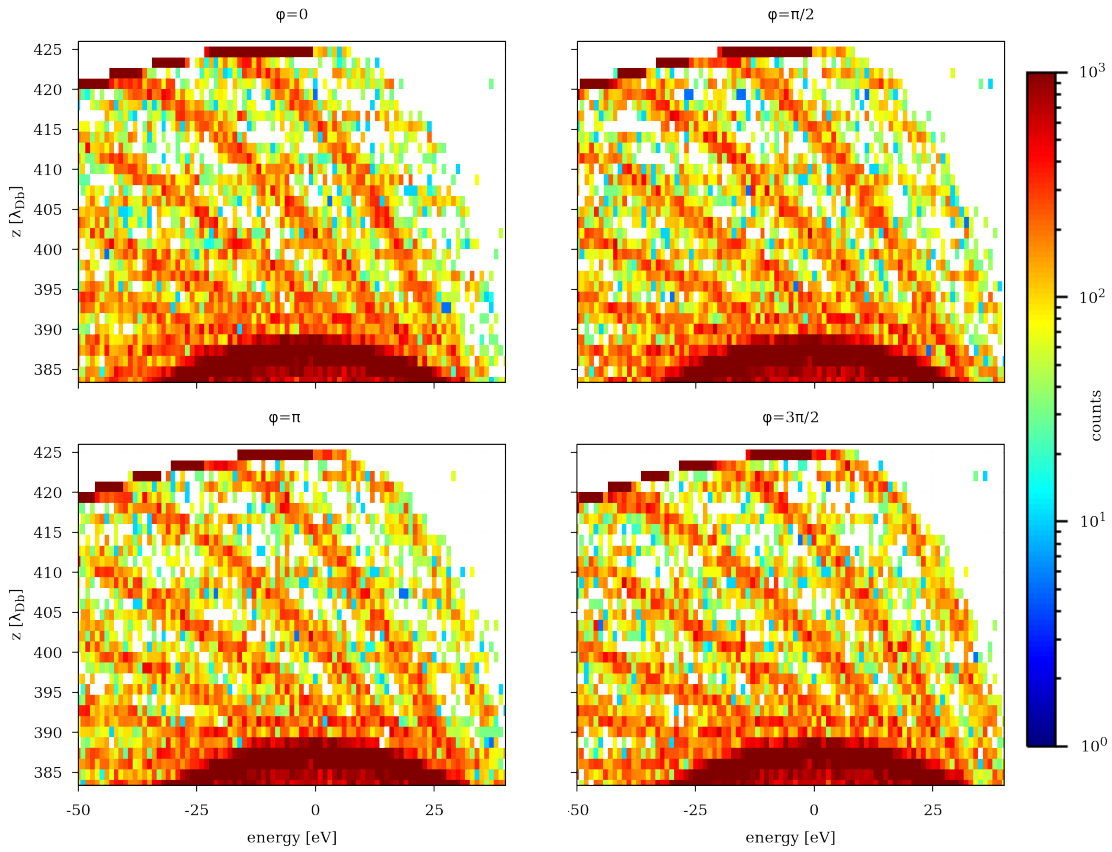

Figure 3.12: Phase resolved surface anion energy distribution functions in front of the cathode.

We have now thoroughly investigated the formation and dynamics of surface produced secondary anions in a 1d3v PIC simulation. It was found that surface ions have a significant impact on the energy distribution function of O^-. However, it was not seen that fast anions created at the surface of the cathode impinge onto the anode. This is due to the intrinsic acceleration in the potential of the sheath, and therefore deceleration in the opposing space charge. One can already tell this from the averaged potential in figure 3.1. A key element to the solution of this problem id the asymmetry of the driven discharge with a self bias voltage. This leads to a stronger acceleration at the cathode than retardation at the anode, and hence to the impact onto the electrode.

The self consistent adjustment of plasma electron and ion current between volume and sheath makes it impossible to implement asymmetry in an one-dimensional simulations. The physics of bulk and sheath are governing the establishment of space charges, as well as the corresponding potential drops towards walls. Like it was discussed by Bronold and Matyash et al. in [1], the key argument for a one-dimensional simulation is the large electrode diameter in comparison to the electrode gap. Here it is said that the plasma properties are not affected, or at least the influence is considered negligible, by the boundaries of the electrodes.

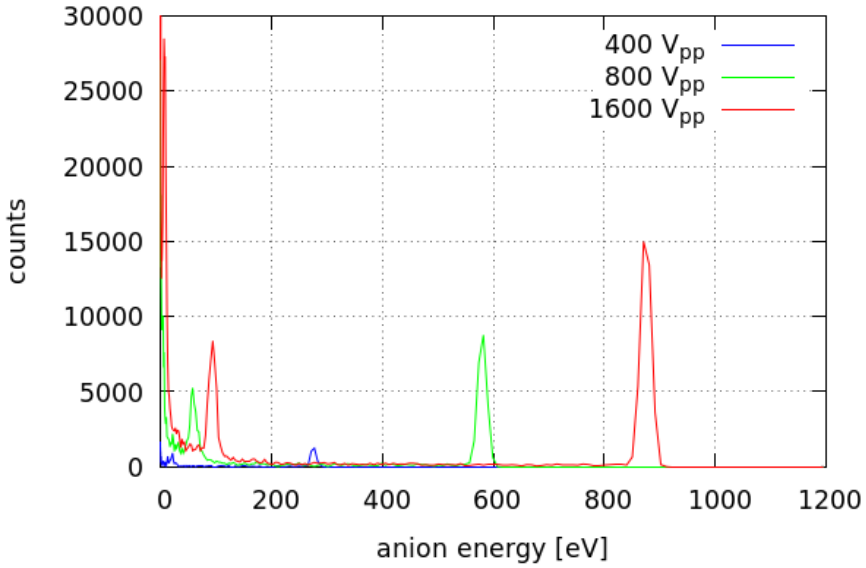

Figure 3.13: Energy distribution of negative ions O^-. Simulation result taken at the anode sheath edge at different rf powers at 5 Pa.

Along the axial centre of the discharge the plasma 'does not see' the edge of the electrodes and therefore no asymmetry effects should take place [12].
From the results found by [19] we know that fast ions can impinge onto the anode. Hence one needs a better model to describe the relevant physics of the experiment. A step towards this solution is the introduction of a two-dimension PIC simulation in which asymmetry effects such as self bias are implemented. The next chapter is devoted to that topic.

Chapter 4

2D Simulation of Capacitively Coupled RF Discharges

After using a 1d3v PIC algorithm to investigate and understand the dynamics of negative oxygen ions in an axial approximation of a symmetrical radio frequency plasma, we will now look at the influence of asymmetry effects in capacitively coupled discharges. Therefore, a 2d3v PIC-MCC simulation is used, where the axial and radial direction is resolved. In this chapter we want to investigate the impact of self-bias and different asymmetry conditions on the development of a plasma, e.g. by varying the area ratios of electrodes and the self-bias voltage. The dynamics and energy distribution of negative ions are discussed in more detail.

4.1 Simulated Discharge

The cylindrical setup in [19] is represented by a 2d3v PIC simulation with two spatial dimensions (r, z) and the full velocity triplet $\vec{v} = (v_\mathrm{r}, v_\vartheta, v_\mathrm{z})$. They form a two-dimensional mesh of grid points in radial and axial direction. Figure 4.1 shows the full cylinder on top of the simulation domain. The cylindrical metrics has to be taken into account for fluxes and densities. A weighting methody proposed by Verboncoeur et al. [25] is used.
Because the radial dimension has been introduced, additional transport occurs in this direction. This additional radial loss of particles compared with the 1D situation requires higher production rates to sustain a stable discharge.

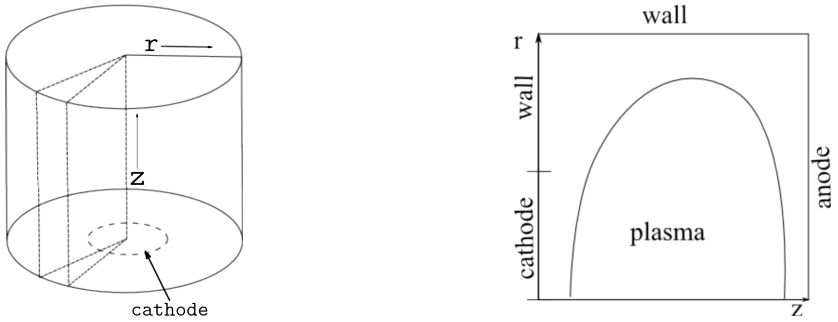

(A) Simulation domain. (B) Plasma bulk and boundary conditions.

Figure 4.1: Cylindrical schematic of the simulated discharge. [12]

In order to realise an asymmetric discharge the area ratio of driven and grounded electrodes are varied. The large area of the grounded vessel walls have to be considered as well. For the self-bias voltage and negative surface ionisation efficiency experimental values from [16, 9] are used.

To assure the validity of this algorithm, we will compare the results of the one-dimensional model with those of the 2d3v simulation. We consider this as sufficient, because the 1D PIC approach is a well-established method and has been widely approved [14, 1, 12]. Subsequently, the influence of different asymmetries, e.g. sizes of driven and grounded electrodes, self bias voltage and secondary ion emission from surfaces on the discharge, will be investigated.

4.2 Validation of Simulation Method by Comparison with 1d3v PIC - The symmetric discharge

The possible solutions in a two-dimensional simulation model are more complex than those of the 1D counterpart. The additional radial transport leads to modifications of the 1D solution and the system is much more sensitive to boundary conditions. A 1D PIC simulation is always intrinsically symmetric, whereas in 2D one has to take care to ensure this. In fact, the possibility for asymmetric solutions is motivating the use of 2D, because this is needed to get more realistic conditions than a 1D code. To highlight this, discharges with different boundary conditions and driver configurations are simulated later on, which then will be compared to the results from the one-dimensional model.

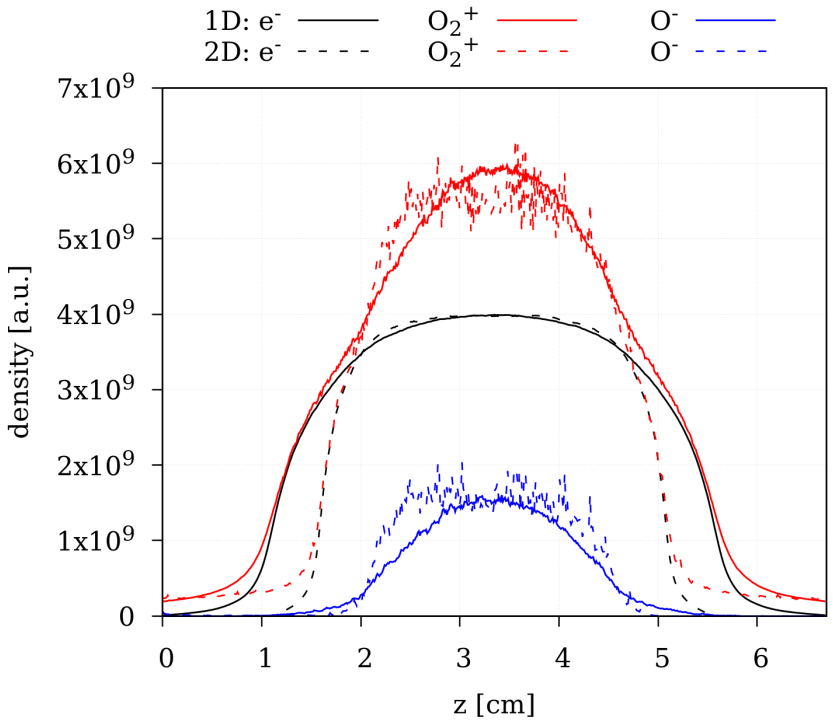

Figure 4.2: Comparison between 1D and 2D results of densities at the axis of a cylindrical discharge at 5 Pa and 400 V

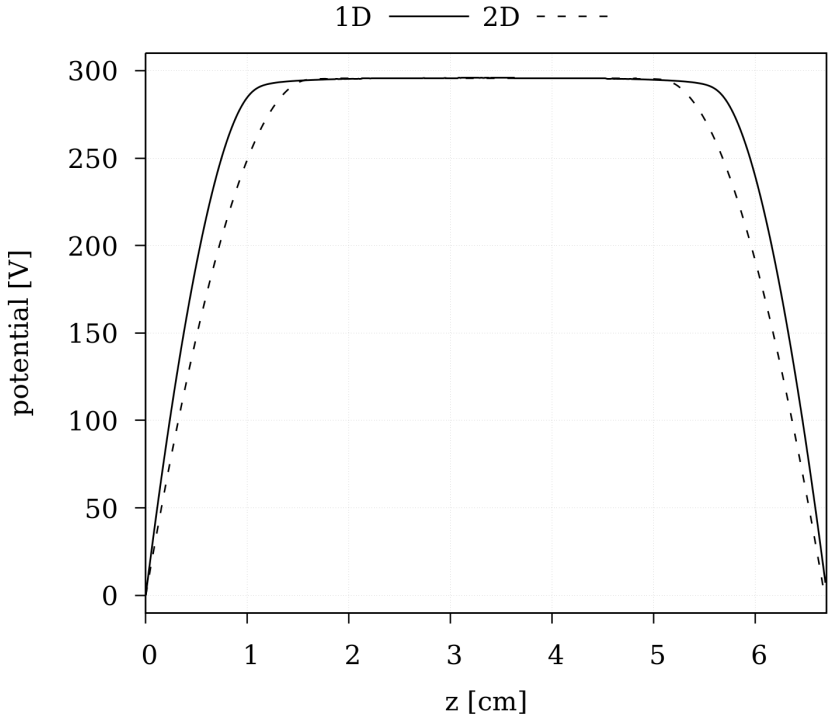

Figure 4.3: Comparison between 1D and 2D results of plasma potential at the axis of a cylindrical discharge at 5 Pa and 400 V

The 1D code is used to simulate the central part of a discharge with a length of 6.72 cm at 5 Pa and a driver voltage of 400 V. Again, negative surface ions are produced at the cathode. The driven electrode is on the right hand side at $z = 6.72$ cm, whereas the anode at $z = 0$ is grounded. The electrodes are mirror-inverted to the 2D case.

First, a fully symmetrical discharge is simulated in 2D. The use of one grounded and one driven electrode does not yield the correct result, which will be discussed later. Instead, one applies an external excitation of 400 V on both electrodes, at $z = 0$ and $z = 574\lambda_{\mathrm{Db}}/2$, respectively, with a difference in phase of π. No self-bias will be introduced. The electrode sizes were chosen to be equal with 2.25 cm at one quarter of the domains radius, which itself was set to 8.98 cm. This corresponds to 175. The electrodes are driven sinusoidally at 13.56×10^6 Hz with 400 V peak voltage. The boundary conditions above the electrodes at the left and right domain boundaries are zero electric field $\vec{E} = 0$. The outer radial boundary is set to ground representing the vessel wall.

A comparison of density profiles and potential is given in figure 4.2 and figure 4.3. The dotted lines show results from the 2D, and solid ones from the 1D simulation. The density and potential profiles in 2D are averaged over a few cells in radial direction, e.g., 20 – 30 cells to reduce the statistical errors.

The bulk densities are in good agreement within their statistical errors in the centre of the discharge, e.g approximately1.8 cm to 5.2 cm. The 2D density profiles have the same features as the 1D ones: the charged species form a well-defined plasma bulk around the centre of the discharge, in which the sum of electron and negative ion density equals the ion density of positive ions.

Differences occur towards the plasma sheaths. The space charge areas for the 2D case are larger in front of both electrodes, approximately $60\,\lambda_{\mathrm{Db}}/2$. Conclusively, the densities decay much faster from the bulk. This is due to the additional influence of the continuity condition for electron and ion flux by the plasma boundaries and electrode edges. They have a great influence on the density and potential, as it was described by equation 1.2. There are additional radial transport processes, which occur in the 2D simulation. They lead to a loss of particles, which is equivalent to an outwards flux. In areas where the confinement in the bulk is no longer given, particles can escape from the plasma.

In figure 4.4 the densities and potential for the full 2D domain is shown. The plasma bulk is shaped self-consistently by the influence of the 2D boundaries. In the logarithmic plot of the electron density the small areas around the whole plasma show up clearly where the density drops rapidly.

Regions with differences of electron, negative and positive ion density are limited

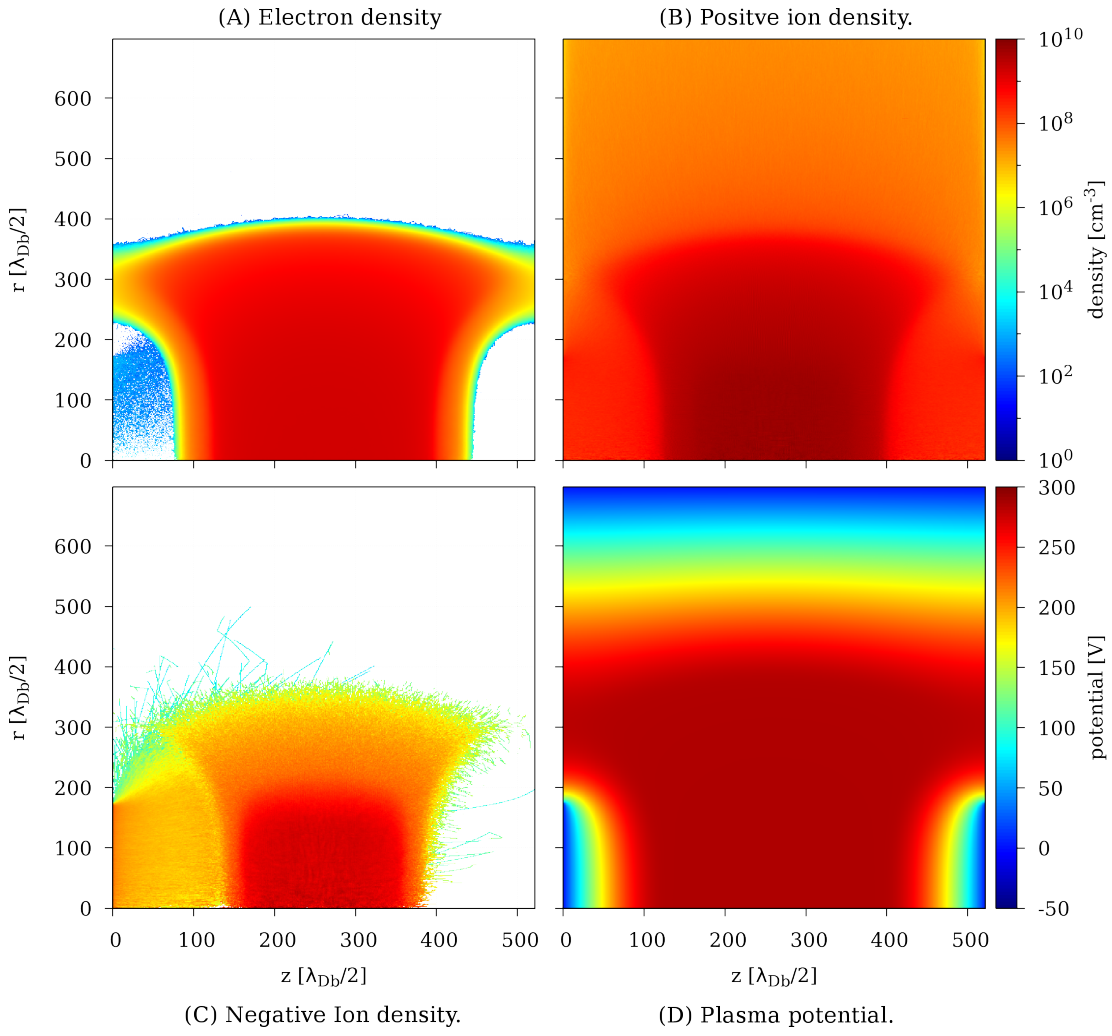

Figure 4.4: Spatially 2D particle densities on a logarithmic scale. Potential of a simulated discharge at 5 Pa and 400 V. The top boundary of the domain is grounded, both electrodes are driven and the remaining parts are allowed to float.

to the plasma sheath: electrons, and eventually the likewise negatively charged ions are depleted in the space charge sheath in front of the electrodes. The positive ions however are accelerated and therefore have a higher density here.
The same surface electron attachment process as described in section 1.5.3 for the 1D simulation is implemented at the left driven electrode. Neutrals hitting the wall can attain an additional electron and are charged negatively. These negatively charged ions are then accelerated within the sheath towards the bulk. They undergo electron detachment within the sheath, so that the electron density in front of the left electrode is increased.
In this symmetric simulation only the left electrode has this surface ionisation process in order to elucidate the influence of this process on the plasma. For the asymmetric case only the left electrode will be driven and consequently the only one with electron attachment. The plasma potential in figure 4.3 is an average

over a few cells from the results shown in figure 4.4. Again, the results from 1D and 2D agree very well. The mean plasma potential is found to be approximately 290 V across the plasma bulk between 1.5 cm to 5.5 cm. However, the voltage drop towards both electrodes is found to be steeper for 2D, which is the consequence of the influence from the boundaries of the plasma and electrode edges.
The potential of the 2D simulation in figure 4.4 very well highlights the findings from before. The mean plasma potential is constant across the bulk. The average potential of the electrodes rest at 0 V, while the grounded part of the vessel on top confines the plasma in the radial direction. The remaining parts of the domain above the electrodes are allowed to float, e.g follow the plasma potential, which implies $\vec{E} = 0$.

In summary, if boundary conditions and symmetry are adjusted accordingly, the 2D code matches the 1D code very well. Therefore the used 2D PIC code can now be used to investigate the influence of asymmetry effects and their impact on the plasma dynamic, not possible in the 1D model. The next section is devoted to the discussion of different boundary conditions with respect to the symmetrical 1D case.

4.3 Influence of Asymmetric Boundary Conditions in 2D

In the following the impact of different combinations of boundary conditions on the development of a low-pressure ccrf plasma is considered. Firstly the same discharge is modelled like in 1D, where one electrode is driven and one is grounded, producing now asymmetry effects. The left electrode is driven sinusoidally with a voltage of 400 V at 13.56×10^6 Hz. Surface processes of negative ions are considered on the cathode. Again, no self bias is applied.
The axial potential profile shows a similar behaviour as the 1D calculations, see Figure 4.5. Differences in the width of the sheath are observed. The corresponding potential drop in the plasma sheath between 0 – 1 cm and 5 – 6.7 cm respectively is also different. In front of the cathode the drop is much steeper than at the anode. Conclusively the sheath is much smaller on that side.
Asymmetries introduced by the different driver configuration are pronounced in the resulting density profiles of the charged plasma species seen in Figure 4.6. Densities are shifted towards the driven electrode at 0 cm.

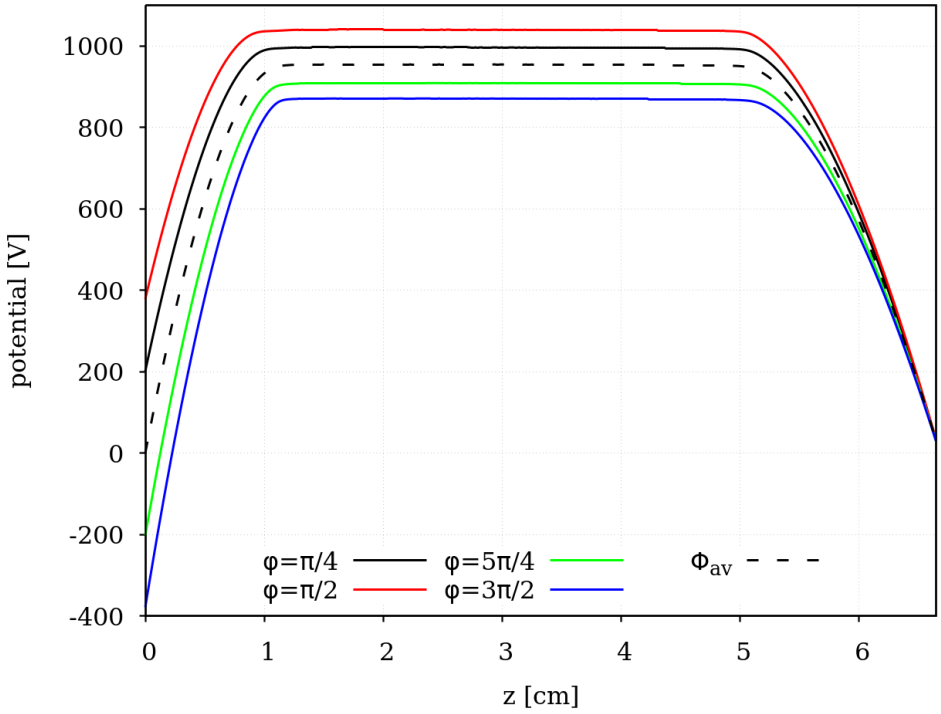

Figure 4.5: Axial profile of plasma potential from 2D simulation at 400 V. Only the left hand electrode at $z = 0$ was driven. It resembles 1D results.

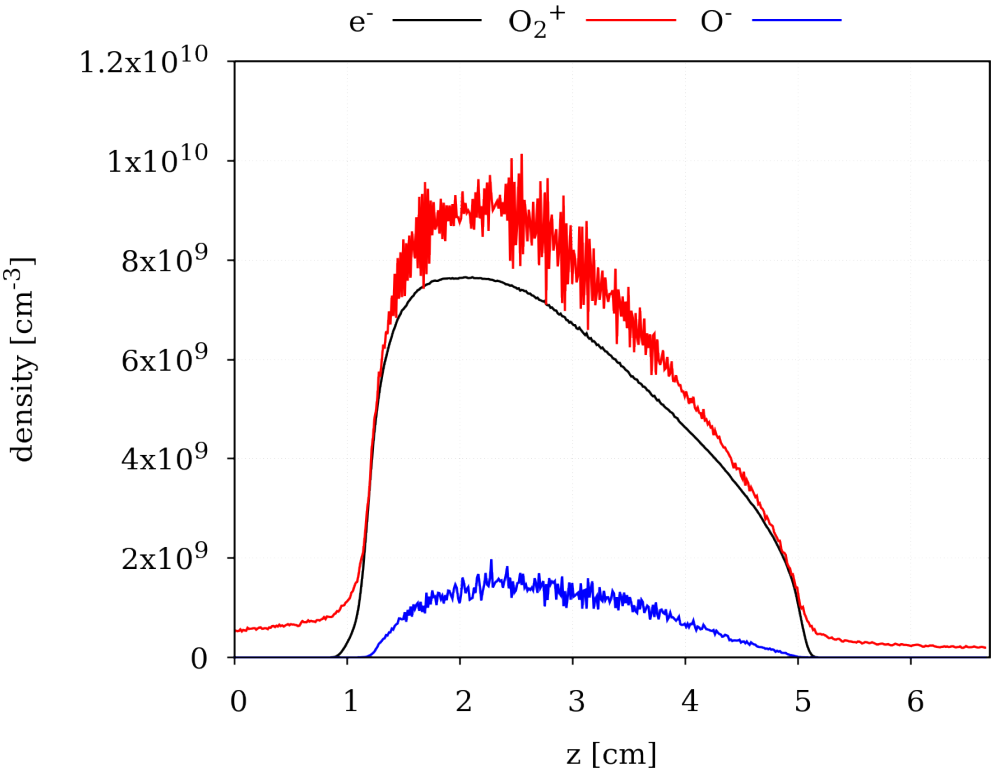

Figure 4.6: Axial profile of densities of the 2D simulation of a discharge at 5 Pa and 400 V. Only the left hand electrode at $z = 0$ was driven, while the other was grounded.

One can easily see the large difference between the ion density in front of the two electrodes. At the cathode n_i is between 3 – 4 times higher than at the anode. This is a consequence of the global asymmetry between the areas of driven and grounded walls. The area of anode and upper wall is much bigger than the area of the driven electrode. Since those are in imbalance, the particle fluxes on the driven electrode need to be higher. The change in the sheath in front of the anode is generated. Therefore different potential drops establish which is shown in figure 4.5. One can see there that also the mean and phase-resolved plasma potential is shifted as a consequence of asymmetry.

By the results of this simulation, where the same boundary conditions like in 1D have been applied, we have seen that an asymmetrical setup yields strong deviations from the earlier results. Plasma potential and densities change according to the global flux condition on grounded and driven walls. Like it was discussed in section 1.1, in a laboratory ccrf discharge asymmetries lead to the development of a self bias voltage. Thus we introduce this property to the 2D simulation. Values are chosen between $-200\,\mathrm{V}$ to $-500\,\mathrm{V}$ from experimental results in [9, 16] and added as a dc-offset to the potential of the driven cathode.

Firstly I will simulate two different asymmetric discharge configurations. The results of potential, ion density and axial ion velocity v_z is shown in figure 4.7. This is only a small selection of the full diagnostics set. A comparison between the axial energy distribution function for all species in those discharges and the remaining densities can be found in figure A.1 through figure A.4. Both discharges were 8.98 cm in diameter and had an electrode gap of 6.72 cm. At a Debye length of 0.0235 cm this resulted in a domain size of $(764 \times 572) \cdot \lambda_{\mathrm{Db}}/2$ in both directions respectively. They were equally driven at a voltage of 400 V and rf frequency of $13.56 \times 10^6\,\mathrm{Hz}$.
The discharge on the left side of the plot panel was driven at the bottom quarter of the left domain boundary, e.g between 0 and 22.7 cm, with an additional $-500\,\mathrm{V}$ self bias. Because the rest of the boundaries were set to ground a large asymmetry sustained, which conclusively resulted in a high dc offset. The one on the right side was powered on both electrodes up to the same height. The left and top part of the boundary where grounded, while the right was allowed to float.
The first two figures in one column show the potential and ion density. The left has an average plasma potential of around 300 V across the bulk. On the cathode however this is equal to the self bias offset. Between 0.5 cm to 5.7 cm and up to

5 cm the bulk core extends. Plasma potential and ion density are shifted towards the cathode. Sheaths in front of both electrodes are also asymmetric. Before the cathode the ion density is higher by at least one order of magnitude, while the space charge is roughly half the size of the opposing sheath. Density and potential drop at the left electrode are obviously quite large, which means that ions are accelerated at this point to match the current onto other compartments of the grounded vessel. Because of the very large ratio between grounded and driven walls, the cathode sheath yields a much stronger ion current pointing outwards, which can be seen the bottom plot of the axial ion velocity. Here one can see that the acceleration is larger and the ions quickly reach the Bohm velocity of around $1.15 \times 10^6\,\mathrm{m\,s^{-1}}$, while this process extends over a greater distance in front of the grounded anode.

The figures on the right side however yield another picture. The plasma core is shifted and bend towards the floating boundary above the right hand side electrode. The bulk establishes between 2 cm to 5 cm, while the height it makes contact with the wall is around 4 cm. The overall density of the ion particles in this discharge is around one order of magnitude smaller.

Potential drops on both sides are again steep, but not as much as for the comparing setup. Also the average plasma potential is found to be between 800 V to 1000 V, which is much higher than the results from before. On the cathode the mean value is again the self bias voltage. The plasma sheaths are around 2 cm in thickness in front of both electrodes. Corresponding ion densities are equal in between the cathode and anode. However, towards the edge of the bulk near the floating wall the density increases again. Besides the shape of the plasma core, the smaller asymmetry in this simulation led to a smaller sheath and overall density, as well as velocities which can be seen on the bottom of the panel. The acceleration of positive ions takes longer and the currents onto both electrodes are lower in comparison to the left discharge.

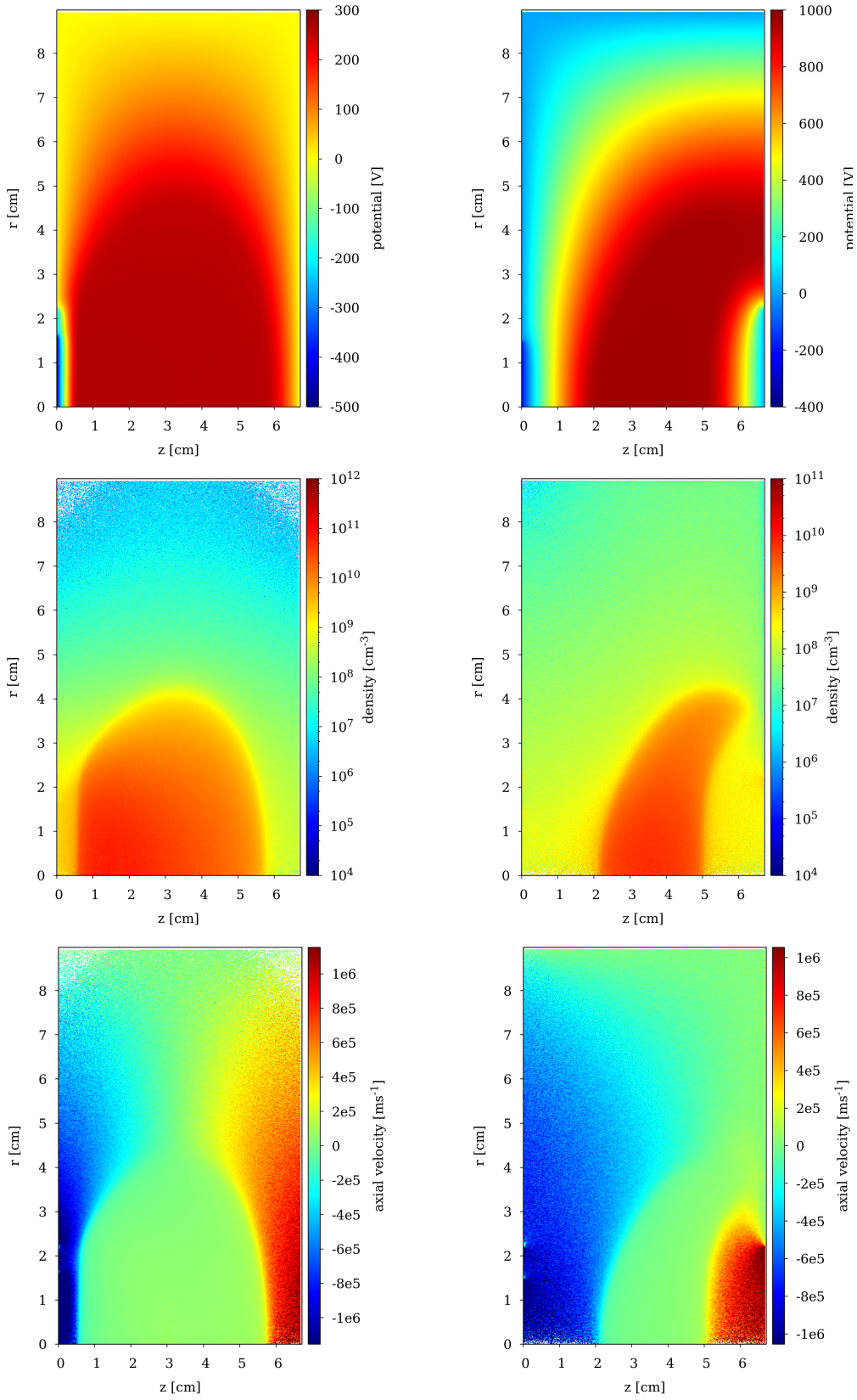

Figure 4.7: Comparison of potential (**top**), ion density (**mid**) and axial ion velocity (**bottom**) for two differently configured discharges. The **left** is driven on the left side and a grounded box is put around it. On the **right** both electrodes are driven, but the top left part is set to ground and the right above the anode is allowed to float. Self bias voltages were $-500\,\mathrm{V}$ and $-400\,\mathrm{V}$ respectively.

4.4 Self Bias and Negative Ion Dynamics

We will now study the dynamics of negative ions in a 2D simulation of rf discharges with a self bias voltage on the driven electrode. The results of this section stand in comparison to the findings from chapter 3, while the introduced self bias is expected to have an important impact on the EDF of negative ions.
The simulation dimensions have been changed slightly. A cathode with a radius of 1.5 cm and an anode with a radius of 4.5 cm is used in the model and a all other boundary conditions are set to ground potential grounded. The electrode gap is about 2.5 cm. We chose an electron temperature of 6 eV and density of $5 \times 10^9\,\mathrm{cm}^{-3}$ for the dimensionless scaling parameters. This gives a cell width of 0.012 cm and a time step of 5.02×10^{-11} s. The corresponding simulation dimensions were 125 cells for the cathode, 375 cells for the anode and an electrode gap of 208 cells.
In figure (4.8) the number density of negative ions is shown for pressures of 10 Pa and 5 Pa with an applied voltage of 400 V. One can see that the bulk region is deformed at the cathode side due to the self-bias voltage of −200 V leading to a reduced electron flux towards the cathode.
There is a higher flux of ions towards the cathode than to the anode due to the self-bias voltage. In the 1D simulation the total ion flux towards the cathode and the cathode sheath are underestimated, because a self-bias effect can not exist. The density distributions have still the same form, where ions are mostly confined in the bulk around the centre of the discharge and their number increases towards the cathode because of an additional particle current from the wall.
In figure 4.9 the axial component v_z of the particle velocity is shown. One can easily see that the negative ions are nearly stationary in the bulk, while at the sheath edges they follow the external electric field. Here they are accelerated in direction of the opposite electrode. At the cathode however the negative ion velocity is much higher than in the bulk or the sheaths. They are are heavily accelerated by an electric field from the excitation and self bias voltage. For lower pressures the probability of energy loss and charge exchange collisions with neutral gas molecules is lower, which is why figure 4.9 at 6 Pa also shows high velocities in front of the anode. Fast surface ions may fly through the bulk because their mean free paths are sufficiently large and impinge on the anode.
To investigate this process we will have a look at the energy distributions of the negative ions. Following the arguments of the one-dimensional model the injected anions should not be able to stay in the discharge, due to the additional energy from the self-bias voltage.

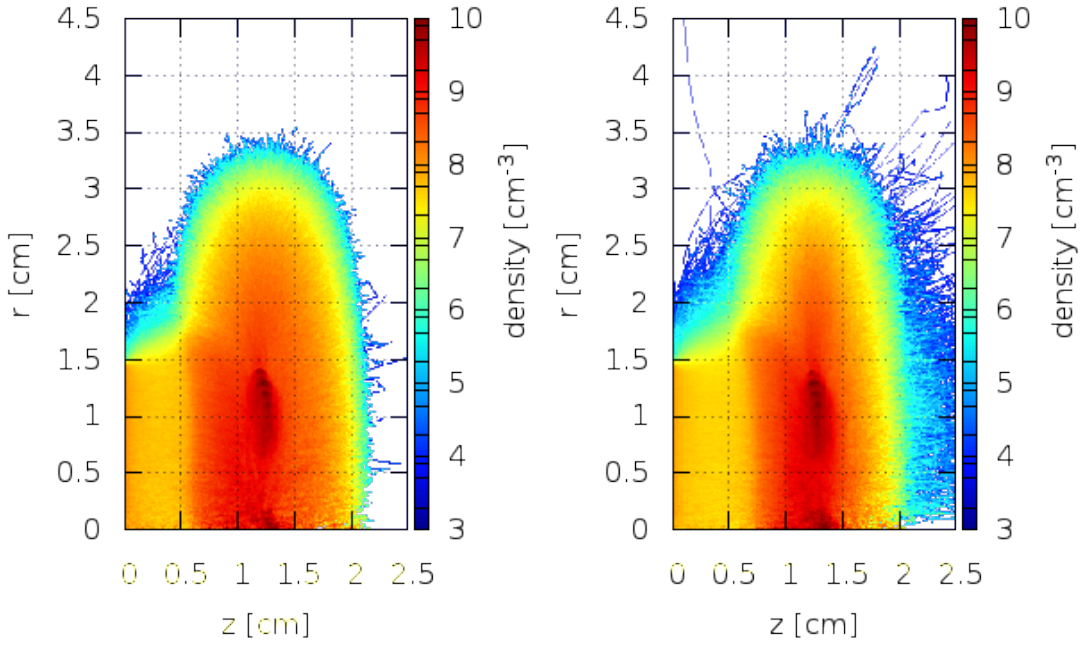

(A) 10 Pa. (B) 6 Pa.

Figure 4.8: Logarithmic plot of negative ion particle density distribution at different discharge pressures.

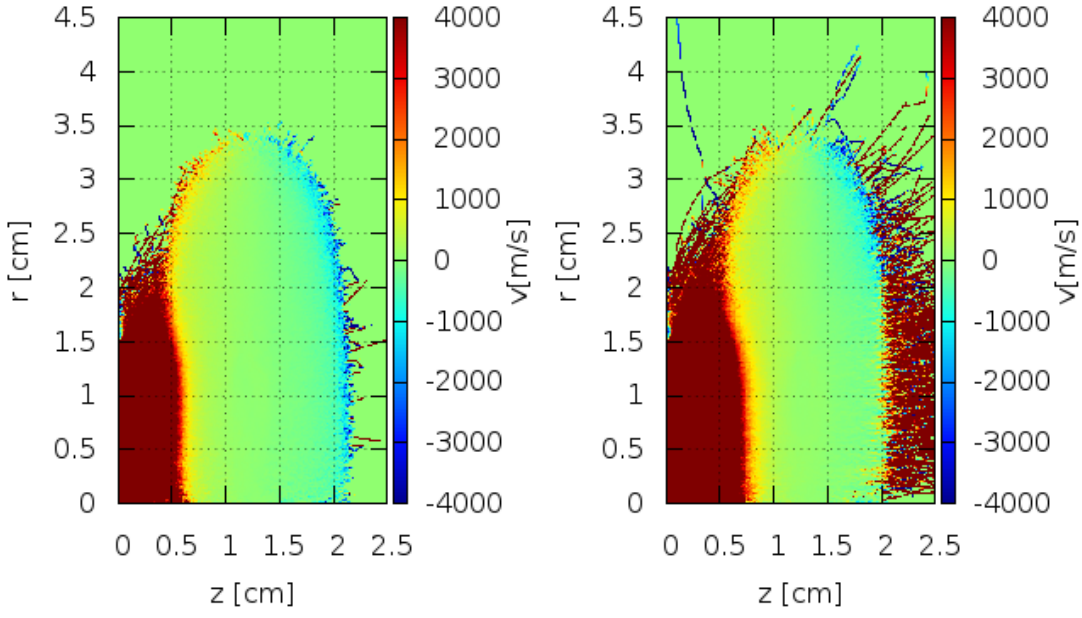

(A) 10 Pa. (B) 6 Pa.

Figure 4.9: Axial velocity v_z of negative ions at different discharge pressures.

In figure 4.10 the EDF of negative ions is shown. Obviously the distribution is strongly asymmetric. A peak structure located at the cathode can be found, which starts around 0 eV and rises to nearly 200 eV when proceeding further along the axis. At 0.7 cm, which is the approximate sheath thickness taken from figure 4.8, the structure reaches the maximum energy. Though the particle counts decrease towards the anode, a non-negligible amount of negative ions reaches the opposing electrode with high energies, e.g >150 eV. This is due to the strong acceleration by an electric field from the combined voltage of self bias and external excitation.

Besides this part of the negative ions species, the majority of particles is found to be at low energies between the discharge sheaths, namely 0.5 cm to 2.0 cm around +/-5 eV. Those slow ions are a result of either volume processes, where low energetic particles are created, or energy loss and charge exchange collisions with low exit velocities. Furthermore, the sheath is found to be collisional, because the peak of accelerated particles already decreases between electrode and bulk. This indicates that energy loss processes can not be neglected there. Similar findings where made in chapter 3, where the number of elastic collisions with min the sheath does no vanish Calculating the negative ion EDF at the grounded anode,

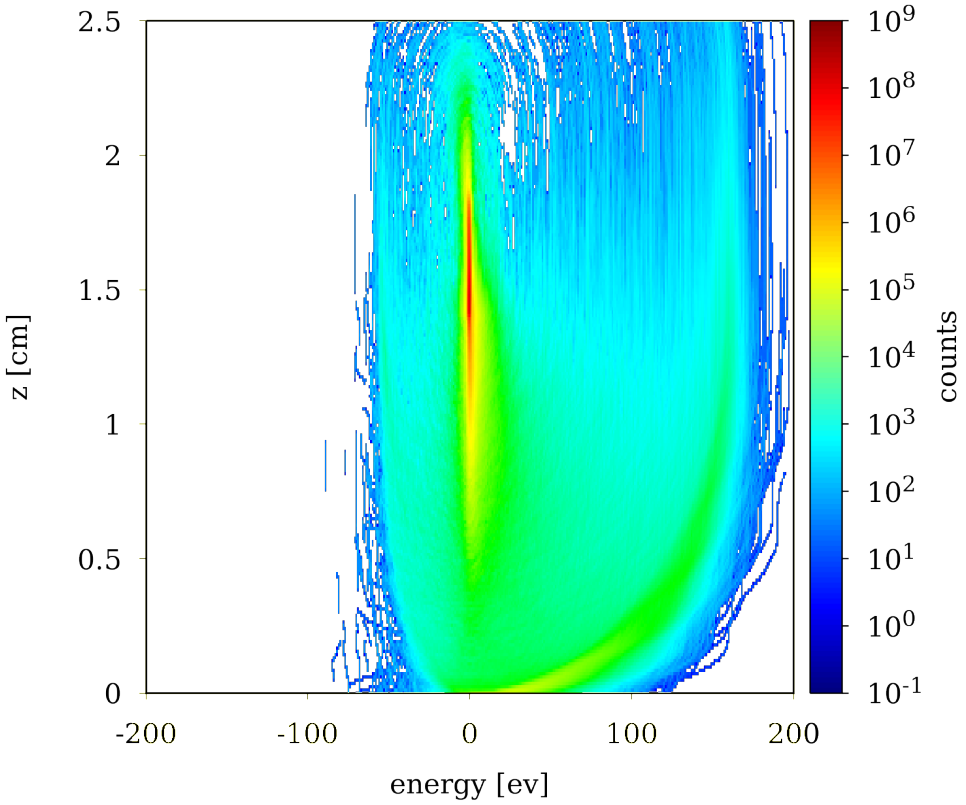

Figure 4.10: Spatio-energetically resolved logarithmic plot of negative ion EDF at 6 Pa and $U_{\mathrm{rf}} = 400\,\mathrm{V}$ and $U_{\mathrm{sb}} = -200\,\mathrm{V}$.

one can compare the results with the experiment. In figure (4.11) the energy of impinging anions at the anode surface for differen self bias voltages is shown. The same high energetic peak can be found as in the experiment. This supports the idea that the observed high energetic peaks in the EDF of the negative ions at the anode in figure 2.3 are produced by surface effects at the powered cathode. This also explains the discrepancy between one-dimensional model and experiment, where an sufficient description of asymmetry and self bias is missing.

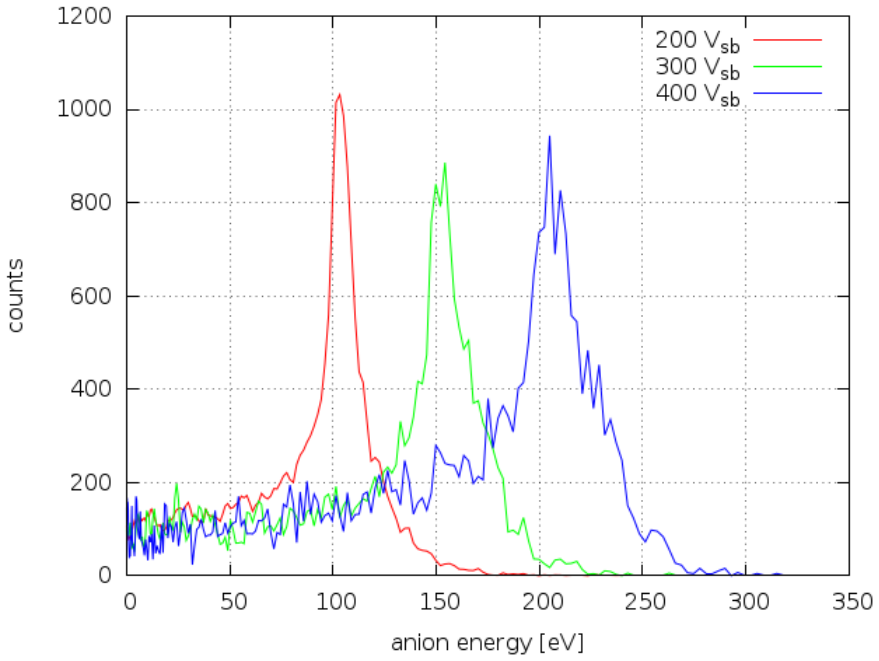

Figure 4.11: Negative ion energy distribution at the anode at 4 Pa and $800V_{pp}$ with different self-bias voltages.

Conclusions

In my thesis I applied a 1D and 2D Particle-in-Cell algorithm including Monte-Carlo-Collisions to simulate a cylindrical low-temperature ccrf discharge at low pressures of oxygen. The goal was to investigate the experimental findings from [19], where highly energetic anions were measured by a mass-spectrometer at the anode of a ccrf oxygen discharge. An explanation is proposed by Stoffels and Kawano et al. [21, 8], suggesting that negative ions are produced by atomic or molecular neutral particles at the electrode surfaces.

A 1D PIC model was used to understand the basic plasma physics and dynamics of negative ions including this surface process at the cathode. An estimate for the efficiency of secondary ion emission was made from experimental results [16]. I was able to reproduce qualitatively the energy distribution function of negative ions, which has a high energy peak due to the acceleration of secondary ions in the plasma sheath. A plateau and an additional low-energy peak in the EDF build up due to energy loss collisions in the bulk and sheath.

However, I was not able to find anions from the cathode to impinge on the anode. This was due to the intrinsic symmetry of a 1D simulation. Hence a 2D simulation model was needed, in which asymmetry effects can occur and a self bias voltage can be applied.

The 2D code was then validated by comparison with the 1D model. It could be shown that both simulations are in good agreement.

In the 2D simulation asymmetrical driven discharges are studied, where cathode and anode configurations are varied and the self bias is introduced. Here, I found that the plasma adjusts self consistently to the different boundary configurations by re-shaping the sheaths and balancing particle currents for the global continuity condition. In case of a highly asymmetric discharge, where the plasma is in contact with a larger area of grounded walls, the sheaths are deformed to match this requirement. They are much larger in front of grounded walls than at a driven electrode. Also the decrease of bulk density and potential is more shallow there. This leads to the reduction of particle densities and velocities inside to

balance the flux.
Accordingly, the EDFs of the plasma species adopt and show the characteristic found in the experiment. Negative ions produced at the cathode can impinge on the opposing anode, because the self bias voltage offset creates an asymmetric acceleration, which lets the anions overcome the potential barrier in front of the grounded wall. The lower energy peak in the EDF of negative ions, which exists in 1D and is seen the experiment, disappears because absorption on the anode is considered.
In summary, with respect to the scientific questions formulated in the beginning of this thesis, I could show that the physics and the dynamics of a ccrf low-pressure oxygen discharg is a complex balance of fast electrons and heavy positive and negative ions. The 1D PIC-MCC gave already a detailed understanding of the physics of this system. However, it lacks the possibility of asymmetries, which are necessary for realistic simulations of experiments. The 2D PIC-MCC code allows this kind of detailed comparison.
This 2D PIC-MCC code gives detailed insight into the second research question, namely to understand the EDF of surface produced secondary particles, like negative oxygen ions. They gain a high energy by a strong acceleration in the sheath. The self bias voltage introduces an asymmetric acceleration of charged particles at the powered electrode. This results in a high particle count of negative ions at large kinetic energies as it is also observed experimentally at the grounded anode. Energy loss and charge exchange collisions lead to the broadening of this peak already in the plasma sheath, which creates a plateau over large ranges of energy. This can be seen in figure 4.10, which is very close to the experimental measurements. Therefore, the two major questions formulated at the beginning of the thesis could be addressed successfully.

In the future, the 2D PIC simulation can be used to study further aspects of asymmetric electronegative discharges, e.g. introducing complex sputter models including chemical reactions. This will also allow to apply it to industrial applications like etching for a more detailed microscopic description. Also, a self consistent approach for the self bias voltage may be implemented. One could measure the flux and accumulated charge locally and thereby calculate an individual dc voltage offset. The displacement current between sheath and bulk is used to approximate the self bias voltage in a balance of inward and outward charge current. Experiments might yield the relevant sheath capacities for the calculation of the self bias. Surface processes are still not very well studied theoretically and experimentally. If here more knowledge exist, emission probabilities for surface processes from theory or experiment can be implemented.

Appendix A

Appendix

A.1 Simulated Energy Distribution Functions from 2D PIC

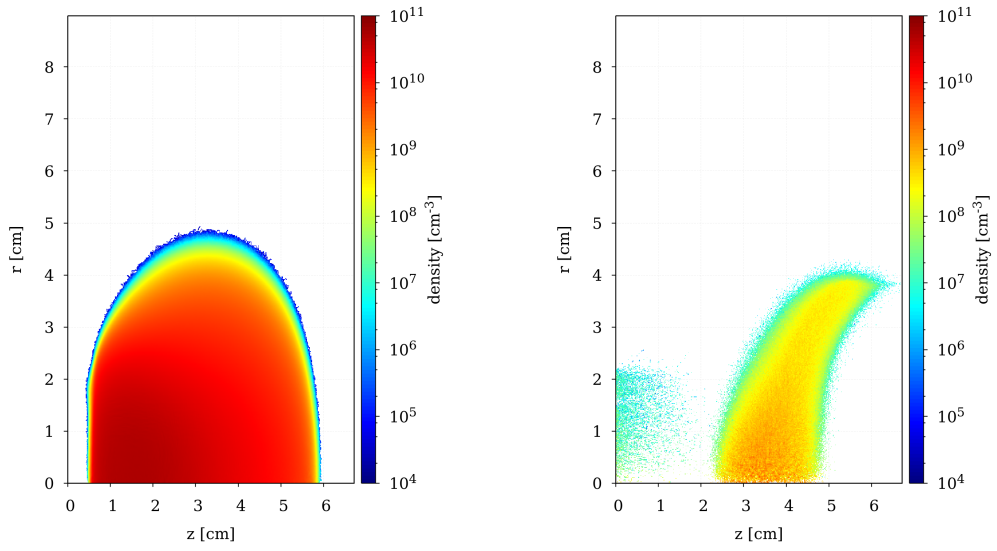

Figure A.1

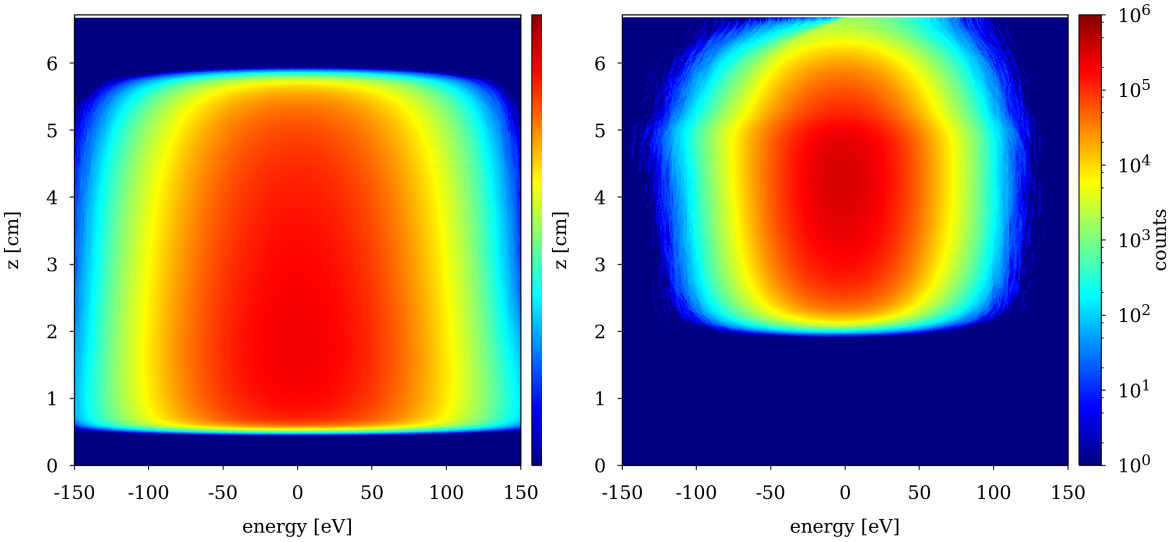

Figure A.2

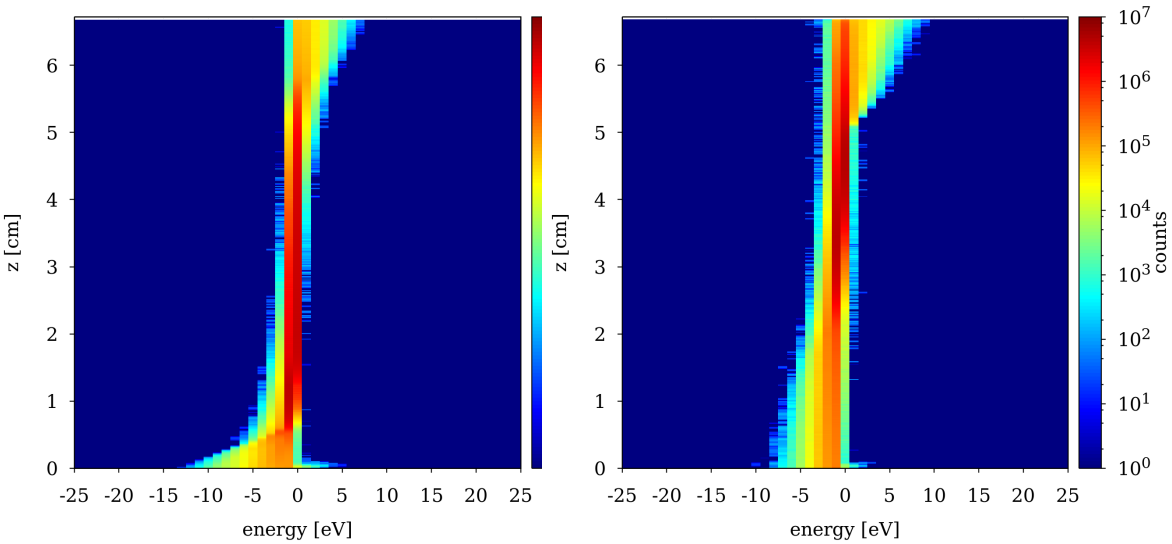

Figure A.3

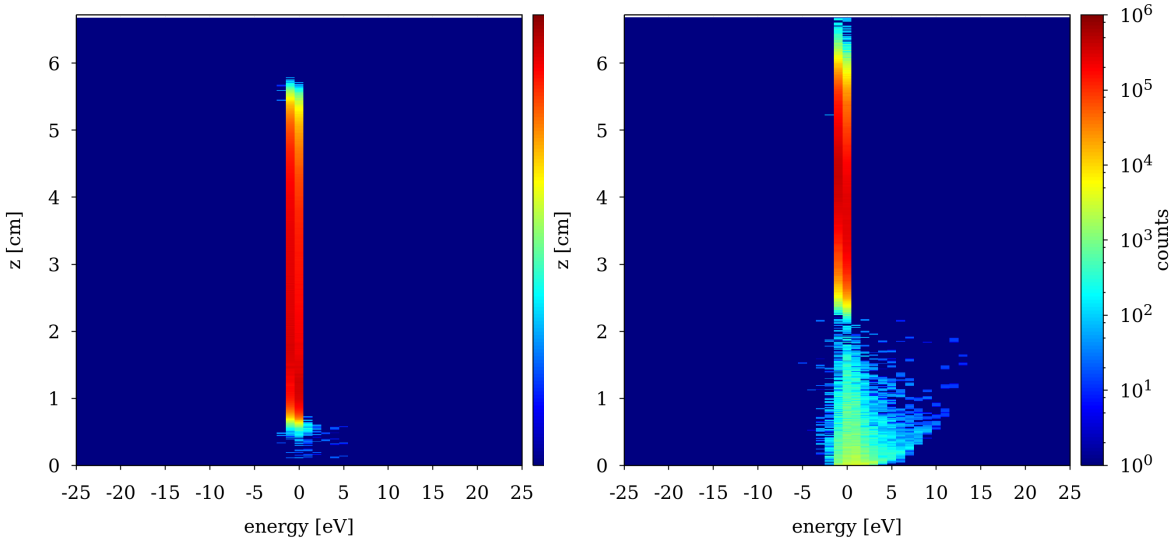

Figure A.4

Physical Properties

quantity	**equation**	**relevance**
Debye length	$\lambda_{\mathrm{D,j}}^2 = \dfrac{\varepsilon_0 k_\mathrm{B} T_\mathrm{j}}{n_\mathrm{j} e^2}$ $\lambda_\mathrm{D}^2 = \left(\lambda_{\mathrm{D,e}}^{-2} + \lambda_{\mathrm{D,i}}^{-2}\right)^{-1}$	distance around a charge, at which quasi-neutrality is satisfied, λ_D is the combined screening length from individual species
plasma parameter	$N_\mathrm{D} = n\dfrac{4}{3}\pi\lambda_\mathrm{D}^3$	number of particles inside Debye sphere, if $N_\mathrm{D} \gg 1$ an ionized gas is considered a plasma (degree of ionization)
plasma frequency	$\omega_{\mathrm{p,j}}^2 = \dfrac{n_\mathrm{j} e^2}{\varepsilon_0 m_\mathrm{j}} = \dfrac{v_{\mathrm{th,j}}}{\lambda_{\mathrm{D,j}}} = \dfrac{1}{\tau_\mathrm{j}}$	upper limit for interaction with fields/forces or external excitations inverse screening time
thermal velocity	$v_{\mathrm{th,j}}^2 = \dfrac{k_\mathrm{B} T_\mathrm{j}}{m_\mathrm{j}}$	mean velocity from kinetic theory of gases
coulomb logarithm	$\ln(\Lambda)$ $\Lambda = \dfrac{b\,\mathrm{max}}{b\,\mathrm{min}} =$ $\lambda_\mathrm{D} \cdot \dfrac{4\pi\varepsilon_0 \mu v_\mathrm{th}^2}{e^2}$	dimensionless scale for transport processes inside discharge fraction of probability for a cumulative 90° scattering by many small pertubation collisions and a single right angle scattering
collision frequency	$\nu_\mathrm{j} = \dfrac{e^4 n_\mathrm{j} \ln(\Lambda)}{8\sqrt{2m_\mathrm{j}}\pi\varepsilon_0 (k_\mathrm{B} T_\mathrm{j})^{3/2}}$	two body coulomb collision frequency inside species j

quantity	equation	relevance
particle distance & mean free path	$\overline{b} = \frac{\hbar}{m_\mathrm{j} v_\mathrm{th,j}}$	mean inter particle distance for species j
	$s_\mathrm{mfp,j} = \frac{v_\mathrm{th,j}}{\nu_\mathrm{j,k}}$	free flight between subsequent collisions of species j and k with collision frequency $\nu_\mathrm{j,k}$
speed of sound	$c_\mathrm{S}^2 = \frac{\gamma Z k_\mathrm{B} T_\mathrm{e}}{m_\mathrm{i}}$ $\gamma = 1 + 2/f = 5/3$	speed of longitudinal ion waves at electron pressure adiabatic coefficient with f, the kinetic degree of freedom
Debye-Hückel potential	$\Phi = \frac{Q}{4\pi\varepsilon\lvert\vec{r}\rvert} e^{-\frac{\lvert\vec{r}\rvert}{\lambda_\mathrm{D}}}$	electrostatic potential of charge particle Q at distance $\lvert\vec{r}\rvert$, equal to coulomb interaction with additional-shielding by charged particles
drift velocity	$v_\mathrm{d,j} = u_\mathrm{j} = \frac{j_\mathrm{j}}{n_\mathrm{j} q} = \frac{m\sigma E}{\rho e f}$	average velocity of a particle in a conductor with an electric field applied E, where N is the number of free electrons per atom
electric mobility	$\mu_\mathrm{j} = \frac{v_\mathrm{d}}{E}$	ability of charged particle of moving through an electric field

Table A.1: Selection of physical properties of a low temperature ccrf discharge. The index j denotes the species, e.g. electrons, ions. Used quantities can be found in the preface in table 2.

List of Figures

List of Tables

Bibliography

[1] F. X. Bronold et al. “Radio-frequency discharges in oxygen: I. Particle-based modelling”. In: *J. Phys. D: Appl. Phys.* 40 (2007), pp. 6583–6592.

[2] U. Cvelbar, M. Mozetic, and M. Klansjek-Gunde. “Selective oxygen plasma etchin of coatings”. In: *Plasma Science, IEEE* 3.2 (2005), pp. 236–237.

[3] V. A. Godyak and S. N. Oks. “Electron energy distribution in a low- pressure rf discharge”. In: *Sov. Phys. Tech. Phys.* (1979), pp. 1255–1256.

[4] V. A. Godyak, O. A. Popov, and A. Kh. Ganna. “Effektive electron collision frequency in rf discharges”. In: *Sov. J. Plasma Phys.* (1976), pp. 560–561.

[5] C. G. Goedde, Allan J. Lichtenberg, and Michael A. Lieberman. “Self-Consistent Stochastic Electron Heating in Radio Frequency Discharges”. In: UCB/ERL M88/29 (1988).

[6] G. Gozadinos et al. “Collisionless electron heating by capacitive radio-frequency plasma sheaths”. In: *Plasma Sources Sci. Technol.* 10.2 (2001).

[7] E. Kawamura J. T. Gudmundsson and M. A. Lieberman. “A benchmark study of a capacitively coupled oxygen discharge of the oopd1 particle-in-cell Monte Carlo code”. In: *Plasma Sources Science and Technology* 22.3 (2013), p. 035011.

[8] H. Kawano and F. M. Page. “Experimental methods and techniques for negative-ion production by surface ionization. Part I. Fundamental aspects of surface ionization”. In: *International Journal of Mass Spectrometry and Ion Physics* 50.1 (1983), pp. 1 –33. ISSN: 0020-7381.

[9] C. Kullig., J. Meichsner, and K. Dittmann. “Detachment-induced electron production in the early afterglow of pulsed cc-rf oxygen plasmas”. In: *Physics of Plasmas* 19 (2012), pp. 73–100.

[10] M. A. Lieberman. “Analytical solution for capacitive RF sheath”. In: *IEEE Transactions on Plasma Science* 16.6 (1988), pp. 638–644. ISSN: 0093-3813. DOI: 10.1109/27.16552.

[11] J. Los and J.J.C. Geerlings. “Charge exchange in atom-surface collisions”. In: *Physic Reports* 190.3 (1990), pp. 133–190.

[12] P. Matthias. *2D Simulation of RF Discharges*. Ernst-Moritz-Arndt Universität Greifswald, Institute of Physics, 2015.

[13] K. Matyash et al. "Particle in Cell Simulation of Low Temperature Laboratory Plasmas". In: *Contrib. Plasma Phys.* 47.8-9 (2007), pp. 595–634.

[14] K Matyash et al. "Radio-frequency discharges in oxygen: III. Comparison of modelling and experiment". In: *J. Phys. D: Appl. Phys.* 40, pp. 6601-6607 (2007).

[15] Konstantin Matyash. *Kinetic Modeling of Multi-Component Edge Plasmas*. Greifswald Universtity, Institute of Physics, 2003.

[16] J. Meichnser et al. "Nonthermal Plasma Chemistry and Physics". In: (2013).

[17] I Okada et al. "Monte Carlo simulation of the reaction and transport of negative ions O - and O 2 - in oxygen". In: *Journal of Physics D: Applied Physics* 11.7 (1978), p. 1107.

[18] A. Piel. "Plasma Physics - An Introduction to Laboratory, Space and Fusion Plasmas". In: (2010), pp. 170 ff., 338 ff.

[19] S. Scheuer. "Plasmadiagnostische Untersuchungen zur Charakterisierung von Moden in elektronegativen RF-Plasmen". In: *Master thesis* (2015).

[20] F. J. Schulze. *Electron heating in capacitively coupled radio frequency discharges*. Ruhr-University Bochum, Fakulty of Physics und Astronomy, 2009.

[21] E. Stoffels, W. W. Stoffels, and G. M. W. Kroesen. "Plasma chemistry and surface processes of negative ions". In: *Plasma Sources Sci. Technol.* 10 (2001), pp. 311–317.

[22] M. Surendra and M. Dalvie. "Moment analysis of rf parallel-plate-discharge simulations using the particle-in-cell with Monte Carlo collisions technique". In: *Phys. Rev. E* 48 (5 1993), pp. 3914–3924. DOI: 10.1103/PhysRevE.48.3914.

[23] D. Tskhakaya et al. "The Particle-In-Cell Method". In: *Contrib. Plasma Phys.* 47.8-9 (2007), pp. 563–594.

[24] S. Ustaze et al. "Electron Capture and Loss processes in the Interaction of Hydrogen, Oxygen and Fluorine Atoms and Negative Ions with a MgO(100) Surface". In: *Physical Review Letters* 79.18 (1997), pp. 3526–3529.

[25] J. P. Verboncoeur. "Symmetric Spline Weighting for Charge and Current Density in Particle Simulation". In: *Journal of Computational Physics* 174, 421–427 (2001).

[26] M. Zeuner et al. "Sputter process diagnostics by negative ions". In: *Journal of Applied Physics* 83.10 (1998), pp. 5083–5086.

Acknowledgements

My utmost and sincere gratitude goes to my thesis chair Prof. Dr. Ralf Schneider and his whole work group. Without their support and advice this would have not been possible. I also would like to say thank you for giving me the chance to work there, which taught me many important things as a physicist and scientist.
A special thanks goes to Stella Scholl, my partner and beloved better half, who supported me no matter the time of day or other circumstances. Without her I would have not made it.
Thank you also to my family, especially my parents and grandparents for always supporting me on my journey. They always backed me up emotionally, mentally and sometimes even professionally.
Last but not least I want to thank my fellow colleagues of the M.Sc. Physics. We made it this far together and this means a lot to me.

"Without encroaching upon grounds appertaining to the theologian and the philosopher, the domain of natural sciences is surely broad enough to satisfy the wildest ambition of its devotees. [...] The work may be hard, and the discipline severe; but the interest never fails, and great is the privilege of achievement."

— John William Strutt, 3rd Baron Rayleigh, 1884
in: Address to the British Association in Montreal